Received: 30 January 2021 | Revised: 6 May 2021 | Accepted: 13 May 2021

DOI: 10.1002/dep2.153

ORIGINAL RESEARCH ARTICLE

The Depositional Record Open Access
A journal of the International Association of Sedimentologists
WILEY

Flow-process controls on grain type distribution in an experimental turbidity current deposit: Implications for detrital signal preservation and microplastic distribution in submarine fans

Daniel Bell[1,2] | **Euan L. Soutter**[1] | **Zoë A. Cumberpatch**[1] | **Ross A. Ferguson**[1] | **Yvonne T. Spychala**[3,4] | **Ian A. Kane**[1] | **Joris T. Eggenhuisen**[3]

[1]Department of Earth and Environmental Sciences, University of Manchester, Manchester, UK

[2]Department of Geoscience, University of Calgary, Calgary, AB, Canada

[3]Department of Earth Sciences, Utrecht University, Utrecht, the Netherlands

[4]Institute of Geology, Leibniz University Hannover, Hannover, Germany

Correspondence
Daniel Bell, Department of Geoscience, University of Calgary, University Dr NW, Calgary, Canada.
Email: daniel.bell1@ucalgary.ca

Funding information
We are grateful to the European Plate Observing System for funding this work through a Transnational Access grant.

Abstract

Deep-water depositional systems are the ultimate sink for vast quantities of terrigenous sediment, organic carbon and anthropogenic pollutants, forming valuable archives of environmental change. Our understanding of the distribution of these particles and the preservation of environmental signals, in deep-water systems is limited due to the inaccessibility of modern systems, and the incomplete nature of ancient systems. Here, the deposit of a physically modelled turbidity current was sampled (n = 49) to determine how grain size and grain type vary spatially. The turbidity current had a sediment concentration of 17%. The sediment consisted of, by weight, 65% quartz sand (2.65 g/cm^3), 17.5% silt (2.65 g/cm^3), 7.5% clay (2.60 g/cm^3) and 5% each of sand-grade garnet (3.90 g/cm^3) and microplastic fragments (1.50 g/cm^3). The grain size and composition of each sample was determined using laser diffraction and density separation, respectively. The results show that: (a) bulk grain size coarsened axially downstream on the basin floor challenging the notion that basin floor deposits fine radially from an apex upon becoming unconfined; (b) no sample composition matched the input composition of the flow, indicating that allogenic signals can be autogenically shredded and spatially variable in sediment gravity flow deposits; and (c) microplastic fragments were concentrated in levee and lateral basin floor fringe positions; however, microplastic concentrations in these positions were lower than input, suggesting microplastics bypassed the sampled positions. These findings have implications for: (a) the development of 'finger-like' geometries and facies distributions observed in modern and ancient systems; (b) interpreting environmental signals in the stratigraphic record; and (c) predicting the distribution of microplastics on the sea floor.

KEYWORDS
environmental signal, heavy mineral, microplastic, signal preservation, submarine lobe, turbidity current

1 | INTRODUCTION

Submarine fans are some of the largest sediment accumulations on earth, and are the ultimate sediment sink for large volumes of terrestrial sediment (Figure 1A; Emmel & Curray, 1983; Mulder & Syvitski, 1995; Talling et al., 2013). Grains of variable sizes, shapes, ages and densities, are transported in rivers from source areas to fans in oceans and lakes (Garzanti et al., 2006; Mason et al., 2017; Webb et al., 2021). Terrigenous organic matter can be incorporated into the sediment load through erosion of soils and land plants, along with anthropogenic pollutants (Figure 1A; Baudin et al., 2010;

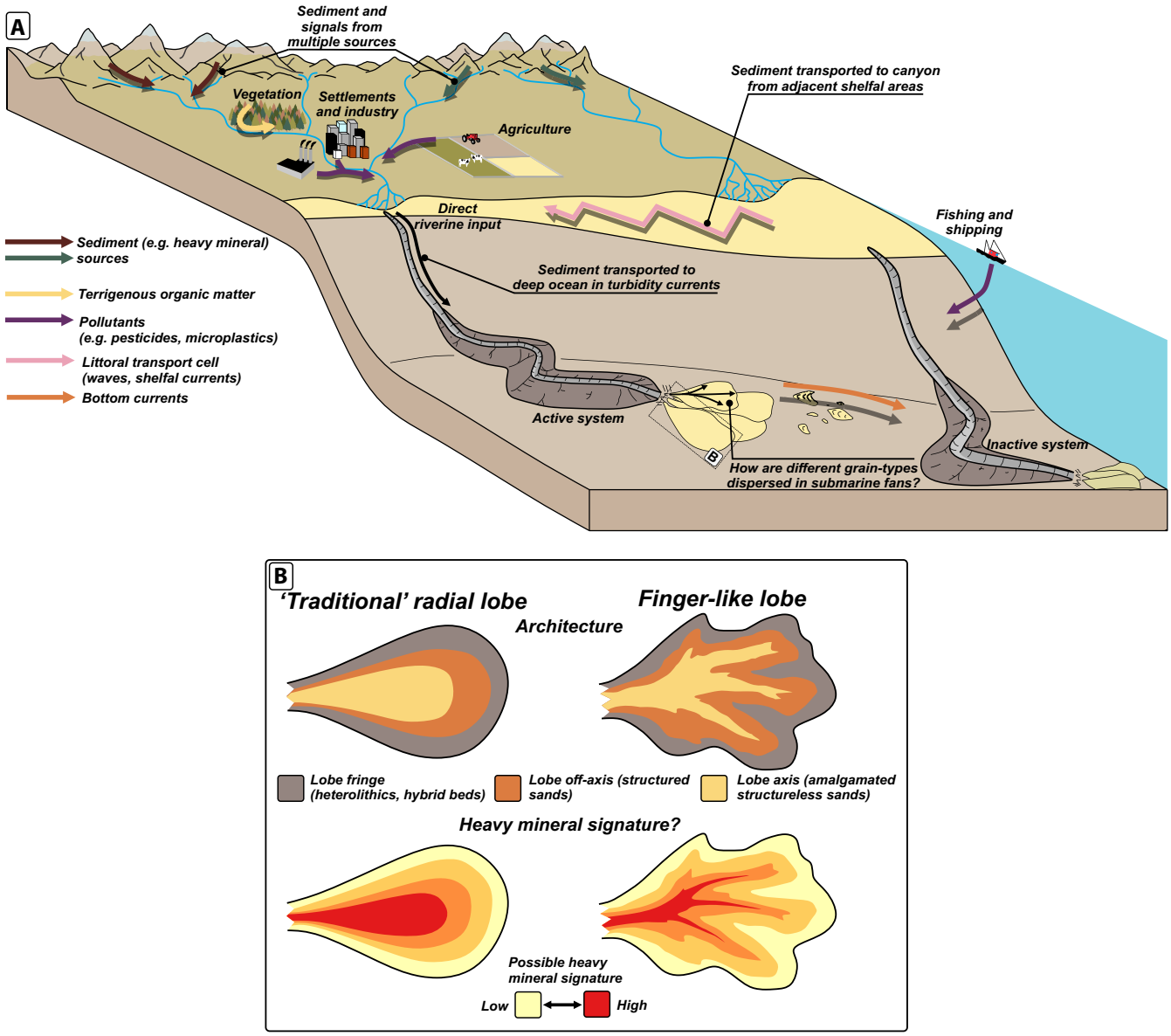

FIGURE 1 Sediment sources and pathways to submarine fans. (A) Conceptual source-to-sink illustration showing pathways for sediment to reach the deep-ocean. Environmental and sedimentary signals include heavy mineral suites, zircons of a given age population, and changing sedimentary fluxes in response to climate or tectonic changes. Such signals propagate from hinterland source areas to the ocean; but can be mixed through sedimentological processes (e.g. river confluences, littoral transport). Sediment loads can also contain terrigenous organic matter affecting the global carbon cycle, and pollutants (i.e. anthropogenic signals). (B) Schematic illustration of how different submarine lobe architectures may affect the spatial distribution of heavy minerals

Galy et al., 2008; Gwiazda et al., 2015; Harris, 2020; Mani et al., 2015). Spatial or stratigraphic changes in the volume, or flux, of these different grain types can be used to infer past environmental changes and signal propagation (Romans et al., 2016). How such grain types are spatially distributed is relatively well-studied in fluvial and shallow marine systems in contrast to submarine fans which are comparatively challenging to monitor and access. This problem is compounded by fundamental differences in transport mechanisms and flow structure. Rivers typically have thin bedload layers, with most sediment in dilute suspension (van Rijn, 1984); whereas sediment gravity flows are often strongly stratified, exhibiting thick bedload layers where sediment concentrations can exceed 10% volume in which hindered settling dominates and both turbulence and bedform development is suppressed (Kuenen, 1966; Lowe, 1982; Paull et al., 2018; Stevenson et al., 2018; Talling et al., 2012). Furthermore, bottom currents can affect submarine gravity flows affecting their depositional architectures, and rework and redistribute extant deposits, affecting grain type distribution (Fuhrmann et al., 2020; Kane et al., 2020; Rebesco et al., 2014; Shanmugam et al., 1993; Stow & Lovell, 1979).

Mineral assemblages, or individual minerals, can be used to ascertain the provenance or age of a depositional system through comparison with potential hinterland source areas (Dickinson & Suczek, 1979; Fontana et al., 1989; Morton & Hallsworth, 1994; Sickmann et al., 2016; Zuffa et al., 1995). These minerals can have different shapes, sizes and densities and are therefore probably fractionated according to their settling velocities (Garzanti et al., 2008). Thus, signals are liable to be distorted or diluted by variable depositional processes and flow conditions (Ibañez-Mejia et al., 2018; Lawrence et al., 2011). While high-density sampling of lithologically similar turbidites can provide reliable formation-scale results (DeGraaff-Surpless et al., 2003), little work addresses how heavy mineral signals are fractionated within different sub-environments of submarine fans (Figure 1B). Similarly, appreciation of the distribution of lighter particles in deep-water systems, such as microplastics and organic carbon, is important in constraining how pollutants are transported and stored in the deep oceans, and global organic carbon budgets (Galy et al., 2007; Gwiazda et al., 2015; Kane et al., 2020; Schlining et al., 2013; Zhong & Peng, 2021). Despite the threat posed to marine ecosystems (Kane & Clare, 2019; Kane et al., 2020; Martin et al., 2017; Sanchez-Vidal et al., 2018; Thompson et al., 2004; Woodall et al., 2014), relatively few studies document microplastic transport and deposition in submarine fans (although see: Kane & Clare, 2019; Kane et al., 2020; Pohl et al., 2020b). Consequently, questions remain regarding where and how microplastics are deposited in deep-water systems.

Traditional models of submarine fans predict radial sediment dispersal patterns upon unconfinement of sediment gravity flows, and an associated thinning and fining of the deposits (Figure 1B; Luthi, 1981; Normark, 1970; Walker, 1966). However, systems often exhibit strong directionality, with deposits forming elongate finger-like deposits (Figure 1B; Dodd et al., 2019; Groenenberg et al., 2010; Klaucke et al., 2004; Twichell et al., 1992). Sediment gravity flows spatially segregate their sediment load according to the density, shape and size of grains (Choux & Druitt, 2002; Hodson & Alexander, 2010; Luthi, 1981; Mériaux & Kurz-Besson, 2017; Pyles et al., 2013), and discrete flow-types carry or deposit these grain types depending on their grain-support mechanisms, which can vary spatially and temporally (Baas et al., 2011; Fildani et al., 2018a; Kane et al., 2017; Stevenson et al., 2014; Talling et al., 2012). The deposits of modern sediment gravity flows have been found to record spatial changes in heavy mineral composition (Andò et al., 2019; McLennan et al., 1989; Sarnthein & Bartolini, 1973; Sickmann et al., 2019); although the challenges associated with sampling modern systems frequently limit the spatial resolution and number of samples taken. These observations translate through geological time to the rock record, where similar observations have been recognised in outcrops (Norman, 1969). However, outcrops tend to be limited by incomplete, short length-scale and two-dimensional exposures.

Physical experiments, both two and three-dimensional, commonly focus on flow processes and architecture of sediment gravity flow deposits (Alexander & Morris, 1994; Baas et al., 2009; Baker et al., 2017; de Leeuw et al., 2016; Garcia & Parker, 1989; Kuenen, 1951; Middleton, 1967; Postma & Cartigny, 2014; Soutter et al., 2021; Steel et al., 2017; Straub et al., 2008). Comparatively few of these studies explicitly document the distribution of different grain sizes and grain types (Choux & Druitt, 2002; de Leeuw et al., 2018b; Luthi, 1981; Mériaux & Kurz-Besson, 2017; Pyles et al., 2013), and those that do often use dilute and finer-grained flows that do not scale well to natural sediment gravity flows (Luthi, 1981; Pyles et al., 2013). Consequently, despite recognition that the distribution of grain types in sediment gravity flow deposits is spatially variable, relatively few studies have described and quantified the distribution of diverse grain type loads.

Here, the spatial distribution of grain size and grain types in deposits of an experimental turbidity current are investigated using a sediment load of quartz sand (2.65 g/cm^3; herein sand), clay (2.60 g/cm^3), silt (2.65 g/cm^3), garnet (3.90 g/cm^3) and microplastics (1.50 g/cm^3). The results are used to answer the following questions: (a) How are different grain sizes and minerals segregated in sediment gravity flow deposits? (b) What can these distributions tell us about turbidity current structure and evolution? (c) How does grain fractionation affect the dilution of a known compositional input spatially? (d) What implications does such a fractionation have for signal preservation and sampling strategies in

submarine fans? And (e) where are microplastics deposited in the deposits of sandy sediment gravity flows?

2 | MATERIALS AND METHODS

2.1 | Experiment set-up

The experiment was carried out using the Eurotank flume at Utrecht University, which has dimensions of 11 m × 6 m × 1.2 m (Figure 2). The design of the basin followed Spychala et al. (2020). From proximal to distal, the floor of the tank consisted of (a) an inlet pipe which discharged the sediment mixtures; (b) a channel 8 cm deep, 80 cm wide and 3 m long with sculpted levees on a slope dipping at 11°; (c) a 4 m long slope dipping at 4° and (d) a 4 m long, flat basin floor (Figure 2). The base of the tank was covered in fine sand, allowing erosion of the substrate by the experimental sediment gravity flows in certain areas.

The flow consisted of 400 kg of sediment which was mixed in a 900 l mixing tank to a concentration of 17 vol% (Figure 2). The sediment mixture was 65% sand (2.65 g/cm^3), 17.5% silt (glass beads; 2.65 g/cm^3), 7.5% kaolinite (1.5 g/cm^3), 5% microplastic fragments, that is not fibres (Urea, Melamine and Acrylic; *ca* 1.5 g/cm^3) and 5% garnet (3.9 g/cm^3). Sand, garnet and microplastics particles were moderately to highly spherical, and angular to sub-rounded. The sediment had a mixed median grain size of fine sand (Table 1; D_{50} of 141 μm), similar to deposits of many ancient and modern deep-water systems (Bell et al., 2018a; Fildani et al., 2018a; Hussain et al., 2020; Jobe et al., 2017; Kane et al., 2017; Marzano, 1988; Porten et al., 2016; Sylvester & Lowe, 2004).

The sediment-water mixture was discharged at 40 m^3/h into the flume tank. The flow velocity was recorded at eight positions in the tank using ultrasound velocity profile (UVP) probes; four in an axial dip-oriented transect spaced every 80 cm (Figure 3; from proximal to distal UVPs 1, 2, 3 and 4), and five in a strike-oriented transect, which includes the most distal UVP of the dip-oriented transect (Figure 3; from right to left with respect to flow direction, UVPs 5, 6, 4, 7, 8). The UVPs were orientated at a 60° angle to the local bed, as a result the data collected are from positions *ca* 10 cm up-dip of the UVP position (Figure 2). UVP probes 5, 6, 7 and 8 were positioned perpendicular to the slope, which probably resulted in the flow intersecting them at an oblique angle, leading to a slight underestimation of the true flow velocity. The flow velocity data of each UVP were time averaged to enable direct comparison of the velocity profile at various locations across the slope.

2.2 | Sampling method

Upon completion of the gravity flow experiment, the tank was drained slowly overnight to limit the development of drainage networks on the deposit. Laser scans were conducted prior to the experiment, and after drainage. These are used to create digital elevation models (DEMs) with a horizontal resolution of 2 × 2 mm to produce a thickness-change map (Figure 3).

Forty nine samples of approximately 10 cm^3 were collected from the sediment gravity flow deposit. The upper 0.1 cm of the deposit was removed prior to sampling in order to sample the sandy-part of the deposit, rather than the silt or clay-prone cap, as per de Leeuw et al. (2018b). This sampling strategy discards the deposits from the waning-flow phase at the end of the experiment, and targets the deposits formed by the body of the quasi-steady turbidity current (Pohl et al., 2020a). As the tank is fully contained, this method also

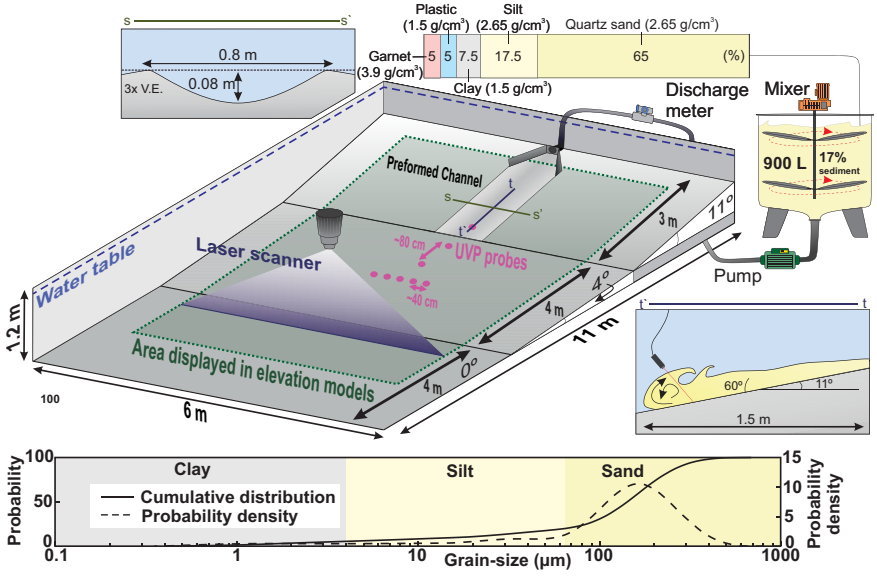

FIGURE 2 Eurotank laboratory and experiment set-up. Adapted from (Ferguson et al., 2020; Soutter et al., 2021)

	Quartz sand	Garnet	Microplastic	Silt	Kaolinite
D_{90} (μm)	239.995	306.667	493.618	112.14	46.94
D_{50} (μm)	161.038	193.349	330.964	52.805	6.511
D_{10} (μm)	107.664	113.819	217.332	0.977	0.977
Coarse sand (%)	0	0	6.956	0	0.042
Medium sand (%)	4.055	17.839	65.23	0	0.026
Fine sand (%)	73.492	67.161	27.812	5.84	0.084
Very fine sand (%)	22.453	13.786	0.002	31.16	3.655
Coarse silt (%)	0.001	0.692	0	25.369	9.871
Fine silt and clay (%)	0	0.523	0	37.631	86.323

TABLE 1 Grain size distribution of grain types used in the experiment

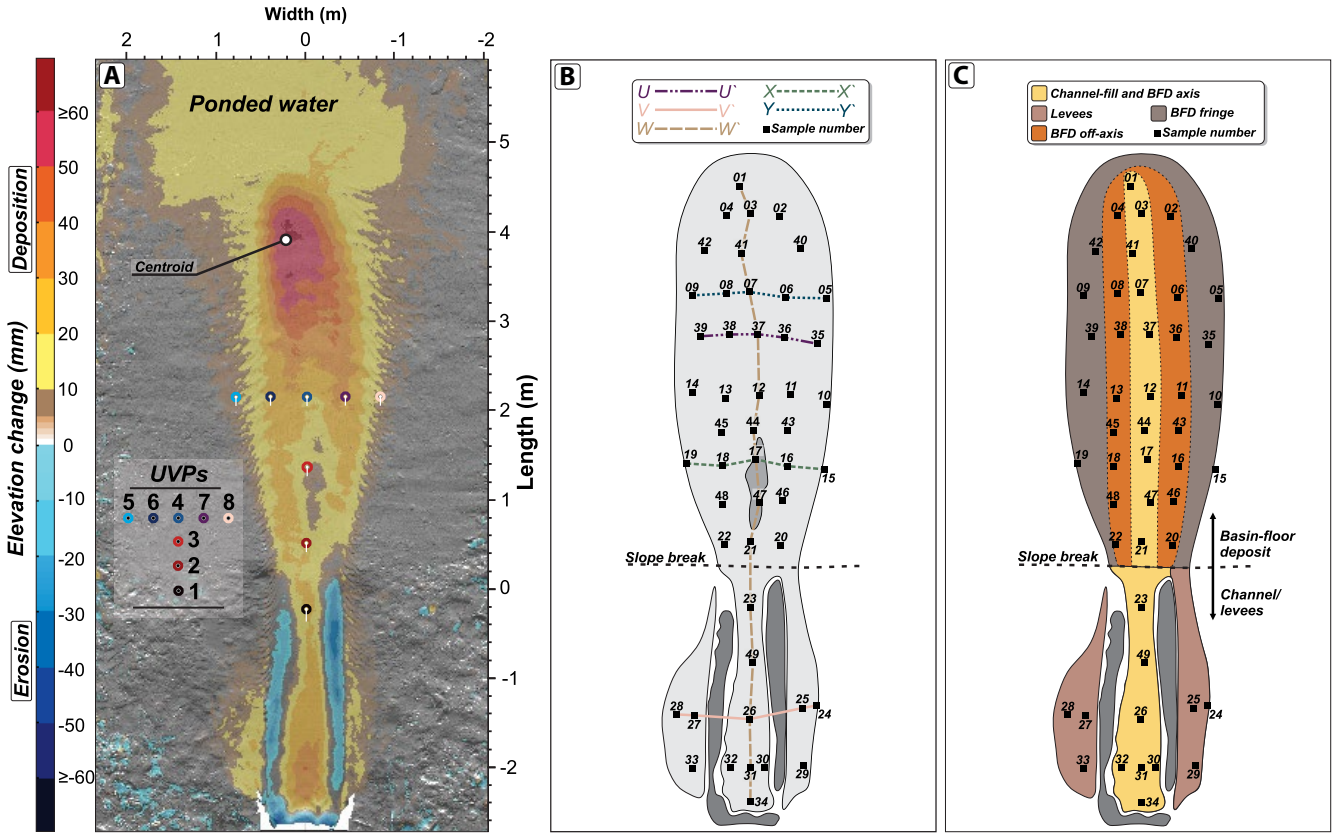

FIGURE 3 (A) Difference map documenting topographic changes pre and post-flow. The distal fringe of the deposit is poorly imaged due to water that ponded on the basin floor during drainage. (B) Sample map showing locations of samples and graph profiles. (C) Sample locations with regard to their associated depositional environment

removes the impact of reflection of the dilute waning flow from the tank walls. Samples were collected from discrete sub-environments (e.g. levees) to constrain spatial heterogeneities in composition and texture (Figure 3C). The basin floor deposit (BFD) was divided into three sub-environments: BFD axis, BFD off-axis and BFD fringe. The BFD fringe deposits are defined by the presence of ripples. Whereas, BFD axis and off-axis sample positions visually appear structureless, and so are pragmatically defined as deposits down the centreline of the flume tank (i.e. directly downstream of the channel mouth), and samples taken laterally away (typically *ca* 40 cm) from the centreline axis, respectively. The tank was laser-scanned after sampling enabling precise identification of sample positions.

2.3 | Grain size analysis

Individual samples were thoroughly mixed using a clean spatula to homogenise grain size and grain types. Sub-samples

were analysed using a Malvern Mastersizer 3000 (Malvern Instruments Limited) and Hydro LV liquid handling unit, using water as the dispersant. The instrument was calibrated using the manufacturer's latex bead quality assurance standard and was within the manufacturers specified tolerances. Samples were subjected to ultrasonic and pre-measurement dispersion. Some samples were analysed more than once to confirm there was no sub-sampling bias, and all samples were analysed five times, sequentially, to confirm there was complete dispersion of the sample. The particle size distribution was modelled using a Fraunhofer estimation model.

2.4 | Grain-type segregation

Grain types were segregated to quantify their spatial distribution. First, the samples were rinsed thoroughly over 63 μm sieves to remove the 'mud' fraction (silt and clay). Sieves were cleaned using an ultrasonic cleaner after each use. The remnant sand, microplastic and garnet mixtures were then separated using LST™ heavy liquid (Central Chemical Consulting Pty Ltd) in a separation funnel. First, garnet was separated from the mixtures using a liquid density of 2.80 g/ml. Second, microplastics were separated from the sand mixture at a liquid density of 1.90 g/ml. Samples were steadily poured into the LST™, after which they were mixed using a spatula. Samples were left to separate for a minimum of 30 min to ensure full separation of grains. The dense and light separations were poured into separate funnels lined with filter paper. Each sample was rinsed with deionised water to remove LST™ prior to drying in an oven and weighing. The LST™ was filtered and recovered after each separation. The coarser fragment of the silt glass beads was able to float during the microplastic separation. To separate this fraction from the microplastics, the mixture was washed through 125 μm sieves using the process described above. The D90 of the glass beads was 112.1 μm, and the D10 of the microplastics was 217.3 μm, which is considered to have enabled an effective separation at 125 μm. After separation, the sub-samples were each weighed using scales with 0.001 g precision, in glass dishes of a known mass, and compared to the original sample weight to calculate weight-percent (wt%).

2.5 | Flow scaling

A Shields scaling approach is utilised as opposed to the Froude scaling approach that was commonly used prior to de Leeuw et al. (2016). The method is based on the relationship between the Shields number (τ^*; Shields, 1936), and the particle Reynolds number (Re_p). The Shields number is defined as:

$$\tau^* = \frac{U^{*2}}{(\rho_s/\rho_f - 1)gD_{50}} \quad (1)$$

where ρ_s is the bulk sediment density (2,705.95 kg/m^3), ρ_f the flow density (1,290 kg/m^3), D_{50} the median grain size (141 μm), g the acceleration due to gravity and U^* is the shear velocity (m/s) as described by Middleton and Southard (1984), and Van Rijn (1993). The particle Reynolds number is defined as:

$$Re_p = \frac{U^* D_{50}}{\nu} \quad (2)$$

where υ is the kinematic viscosity of fresh water at 20°C. The advantage of the Shields scaling approach is that it enables validation that sediment was transported by suspension in the flow, which is not guaranteed with a Froude scaling approach (Fernandes et al., 2020; de Leeuw et al., 2016). Similarly, the Shields scaling approach allows for characterisation of the boundary roughness at the base of the flow (Fernandes et al., 2020; de Leeuw et al., 2016). If the boundary is smooth, there is a thin, laminar layer which prevents particles from interacting with the turbulence in the overriding flow. In a transitionally rough regime, turbulent eddies can interact with the boundary, although viscous forces still exert some control. Natural turbidity currents typically exhibit transitionally rough boundary layers and are above the initiation of suspension threshold (Fernandes et al., 2020; de Leeuw et al., 2016). Shields scaling revealed the bulk experimental turbidity current was transitionally rough (Soutter et al. 2021), and above the suspension threshold in the channel and on the basin floor, and therefore analogous to natural turbidity currents in accordance with the most recent scaling techniques. Such scaling methods are developed using flows comprising quartz sand and calculated for the bulk flow. As such the behaviour of each grain type is more challenging to determine. Garnet is denser than quartz and has a greater settling velocity for a given grain size (Figure 4), and therefore may have been confined to the basal layers and moved as bedload. Conversely, microplastics are less dense than quartz and have lower settling velocities (Figure 4), and therefore probably remain in suspension at lower flow velocities.

3 | RESULTS

3.1 | Deposit geometry

At the inlet pipe exit, there was an area of erosion as the flow met unconsolidated substrate and became relatively unconfined. Beyond this area of erosion the flow became net-depositional along the channel profile (Figure 3). In the channel, the deposit was thickest (4–5 cm) 2 m up-dip of the break-of-slope and thinned gradually down-dip to 1–2 cm at the break-of-slope (Figure 3). The thickest deposits in the channel were in the axis, and deposits thinned towards the

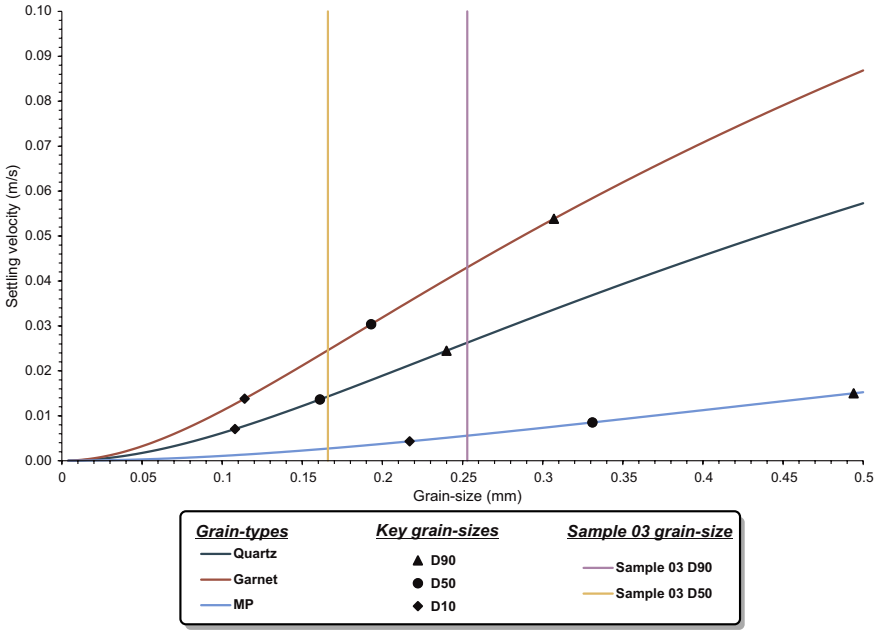

FIGURE 4 Plot of settling velocity against grain size for each sand-grade grain type. Key grain size intervals for each grain type are marked (D_{10}, D_{50} and D_{90}), along with the D_{50} and D_{90} of distal axial sample 03. Settling velocities were calculated according to the method of Ferguson & Church (2004), using a flow density of 1,290 kg/m^3

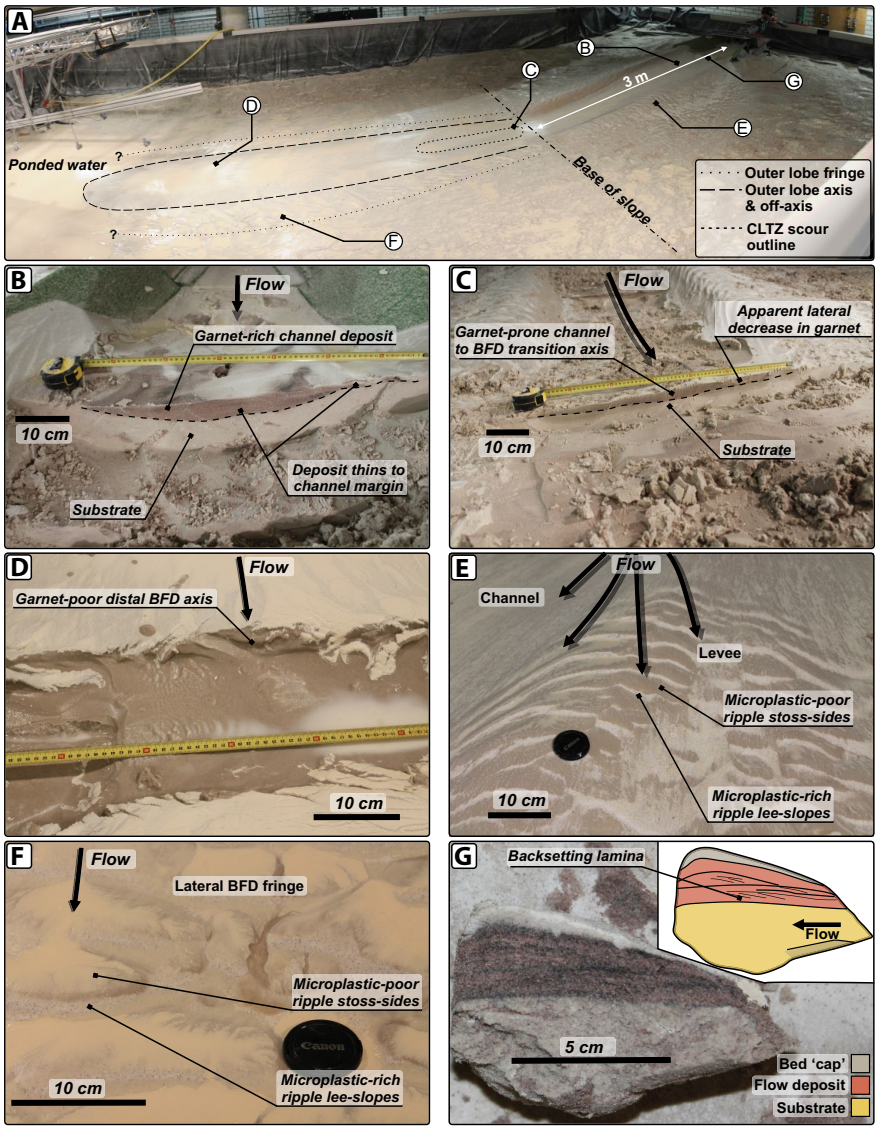

FIGURE 5 Flow deposit geometry and sedimentological features. (A) Overview of the flow deposit and flume tank. (B) Cross-section of deposit in the channel axis. (C) Cross-section of the deposit in the channel to BFD transition zone, immediately down-dip of the break-of-slope. (D) Cross-section of deposit in the distal, axial area of the deposit. (E) Current ripples developed on channel levees. Microplastic fragments (white) were concentrated on lee slopes. (F) Current ripples with microplastic-rich lee slopes in the lateral fringe of the BFD. (G) Garnet-rich backsets developed near the inlet box

channel margins which were predominantly eroded by up to 4 cm (Figures 3 and 5). Outside of the channel, up to 3 cm of sediment was deposited on the levees, which generally thinned with distance away from the channel.

Beyond the channel, the experiment produced a 460 cm long lobate BFD (Figures 3 and 5). Immediately down-dip of the channel, the deposit was relatively thin (<3 cm), and gradually thickened down-dip to a maximum thickness (centroid) of 6.5 cm, 390 cm from the slope break. The deposit widened from 80 cm at the base-of-slope, to 200 cm at a distance of 280 cm from the slope break. Between distances of 80 and 160 cm from the slope break there is a 50 cm wide anomalously thin zone (*ca* 1 cm thinner than the surrounding deposits), similar to convex indents described by Spychala et al. (2020), interpreted to represent a bypass-dominated area in a channel to BFD transition zone (Figures 3 and 5). At the centroid, the axis of the deposit was >5 cm thick for a width of *ca* 80 cm. From the axis the deposit thinned to <2 cm over a *ca* 20 cm distance leaving thin, laterally extensive margins on a metre-scale. The margins of the deposit were dominated by ripples (Figure 5E,F).

3.2 | Flow velocity measurements

The maximum recorded time-averaged velocity, 1.09 m/s, was in the channel at UVP 1 (Figure 3). Flow velocity gradually decreased down-dip from the channel mouth to 0.77 m/s at the most distal axial probe (UVP 4; Figure 6). Although there was a slight increase in flow velocity from UVP 2 at base-of-slope (0.95 m/s) to UVP in the anomalously thin zone (1.00 m/s; Figure 6). Flow velocity decreased abruptly laterally away from the flow axis (UVP 4) to positions off the axis of the flow (UVPs 5, 6, 7, 8; Figure 6). Off-axis UVPs 6 and 7 had flow velocities of 0.54 and 0.72 m/s, 40 cm to the right and left of the flow axis relative to flow direction, respectively (Figure 6). The most lateral UVPs, UVPs 5 and 8, had flow velocities of 0.21 and 0.31 m/s, 80 cm to the right and left of the flow axis relative to flow direction, respectively (Figure 6). UVP probes 5–8 were aligned straight up-slope, oblique with respect to the oncoming flow, therefore the measured velocities from these probes may have slightly underestimated true flow velocity.

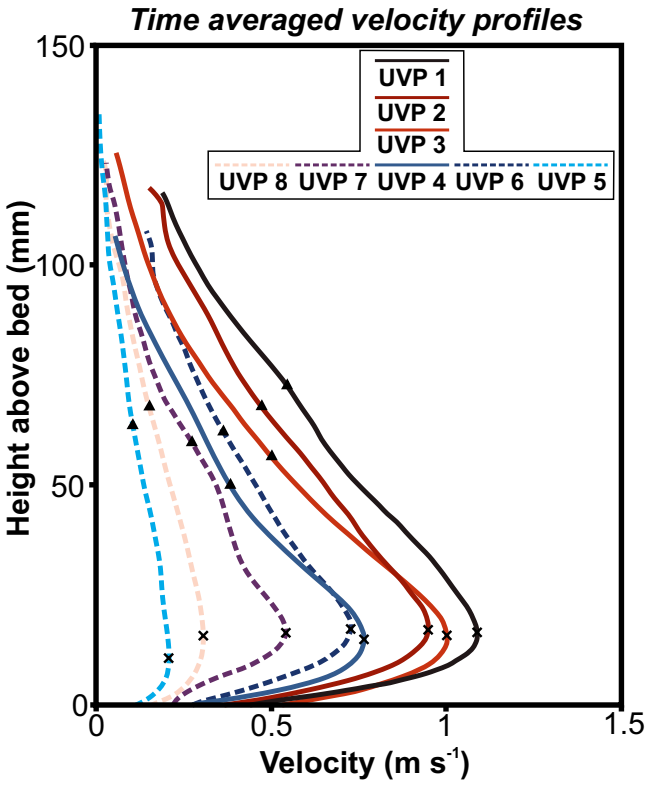

FIGURE 6 Time-averaged velocity profiles from UVPs organised in an inverted 'T' shape. Flow velocity decreases both laterally and longitudinally, although is comparatively abrupt laterally (e.g. UVP 4 to UVP 7 is 40 cm, UVP 1 to UVP 3 is 160 cm)

3.3 | Grain-type distribution

3.3.1 | Microplastic fragments

Qualitative observations suggested microplastics were concentrated in ripple deposits of the levees and BFD fringes, where the lee slopes were enriched in microplastic fragments compared to the stoss slopes (Figure 5E,F). The highest and lowest recorded weight-percentages of microplastic were 1.338 wt% at S10 in the lateral BFD fringe, and 0.007 wt% at S17 and S31, in the channel axis and CLTZ, respectively (Figures 7 and 8); substantially lower than the input of 5 wt%.

The distribution of microplastics was spatially variable in the deposit. In the channel and levees the highest microplastic concentrations were recorded in levee positions. Channel-axis position S26 contained 0.048 wt% microplastic (Figure 7). Levee positions S25 and S27, 20 cm lateral to S26, contained 0.227 and 0.099 wt% of microplastic, respectively (Figure 7). Levee positions S24 and S28, 40 cm laterally away from S26, contained 0.723 and 0.710 wt%, respectively; an increase of 1,408% and 1,382% with respect to S26 (Figure 7).

In the BFD, microplastics were most abundant in fringe positions, and least common in axial positions (Figures 8 and 9). For example, BFD axis position S37 contained 0.030 wt% microplastic; whereas, BFD off-axis positions S36 and S38 contained 0.036 and 0.065 wt% microplastic 20 cm to the right and left of S37, respectively (Figure 7). In contrast, BFD fringe positions S35 and S39 contained 1.185 and 0.393 wt% microplastic 40 cm to the right and left of S37, respectively, representing increases of a factor of 39 and 12 with respect to S37 (Figure 7). No strong trend was identified longitudinally in the BFD axis, with microplastic typically accounting for <0.1 wt% of samples (Figure 8). However, microplastic abundance almost doubled from 0.088 to 0.172 wt% between S03 and the most distal sampled position of S01. Microplastic

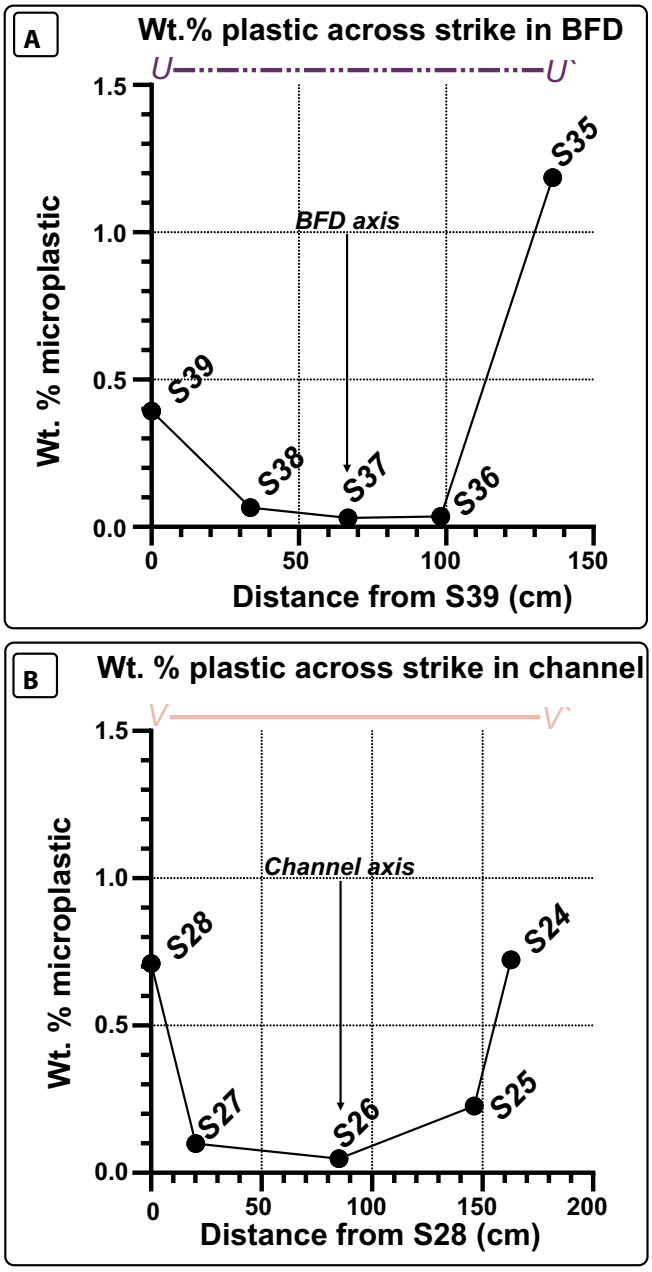

FIGURE 7 Graphs of microplastic particle distribution in the deposit, profiles located on Figure 2B. (A) Across strike profile of BFD. (B) Across strike profile of the channel fill and levees

was locally abundant away from the axis of the CLTZ, where off-axis samples S20 and S22 contained 0.225 and 0.219 wt% microplastic, respectively; in contrast, the comparative axial position of S21 contained 0.017 wt% microplastic (Figure 8).

3.4 | Garnet

Garnet consisted of between 54.7 and 0.1 wt% of samples, recorded in the channel axis at S34 and lateral BFD fringe at S19, respectively (Figure 10); the original flow composition was 5.0 wt% garnet (Figure 11).

Garnet concentration progressively decreased down-dip in the channel from 54.7 wt% at the inlet box (S34) to 13.3% just before the break-of-slope (S23); a 76% decrease (Figures 8 and 10). Garnet abundance exhibited abrupt changes across-strike from the channel to the levees (Figures 8, 10 and 11). From 28.0 wt% in the channel axis position of S26, garnet abundance decreased to: (a) 7.7 and 2.3 wt% at S27 and S28, decreases of 73% and 99%, respectively. And (b) and 3.2 and 2.6 wt% at S25 and S24, decreases of 88% and 91%, respectively; on the left and right levee with respect to flow direction (Figure 10).

In the BFD the highest recorded garnet concentration, 10.9 wt% was recorded in the axis of the BFD at S12, immediately down-dip from the CLTZ (Figure 10). Garnet concentration was relatively high in proximal axial positions, with positions S21, S47, S17, S44, S12 and S37 (proximal to distal), all exhibiting garnet concentrations of 7.5–11.0 wt% (Figures 10 and 11). Beyond position S37, which had a concentration of 9.3 wt%, the garnet concentration decreased abruptly (Figures 10 and 11). Position S7, 49 cm down-dip of S37 had a garnet concentration of 2.4 wt%; and positions S41, S03 and the most-distal sample, S01, had concentrations of 1.3, 0.7 and 0.2 wt%, respectively (Figure 10).

Strong lateral trends were observed in the BFD. Away from the BFD axis the garnet concentration decreased abruptly over relatively short distances (Figures 8 and 10). For example, the garnet concentration at axial position S17 was 10.3 wt% (Figure 10). The garnet concentration of the equivalent off-axis positions to the left (S18), and right (S16), decreased to 2.5 and 2.6 wt% over distances of 39 and 36 cm, respectively (Figure 10); representing decreases of 79.4% and 74.9%, respectively. The lowest garnet concentrations were recorded in the lateral BFD fringes (Figure 9), where the garnet concentration decreased to 0.10 wt%, and 0.14 wt%, at S19 and S15, on the left and right lateral fringes of the transect, respectively (Figure 10); both decreases of 99% with respect to the BFD axis. A similar trend was observed in distal BFD positions, albeit with lower axial concentrations. Garnet abundance decreased from 2.4 wt% at axial position S07, to 1.1 and 0.9 wt% at S08 and S06 in off-axis positions, and 0.2 and 0.3 wt% at S09 and S05 in lateral fringe positions (Figure 10).

3.5 | Grain size distribution

Grain size distribution was spatially variable in the flow deposit, although the median and mean grain size of all deposits was classified as lower fine sand (Figure 12).

3.5.1 | Median grain size distribution (D_{50})

The finest median grain size, 130 μm, was recorded in the lateral BFD fringe at S19, whereas the coarsest D_{50},

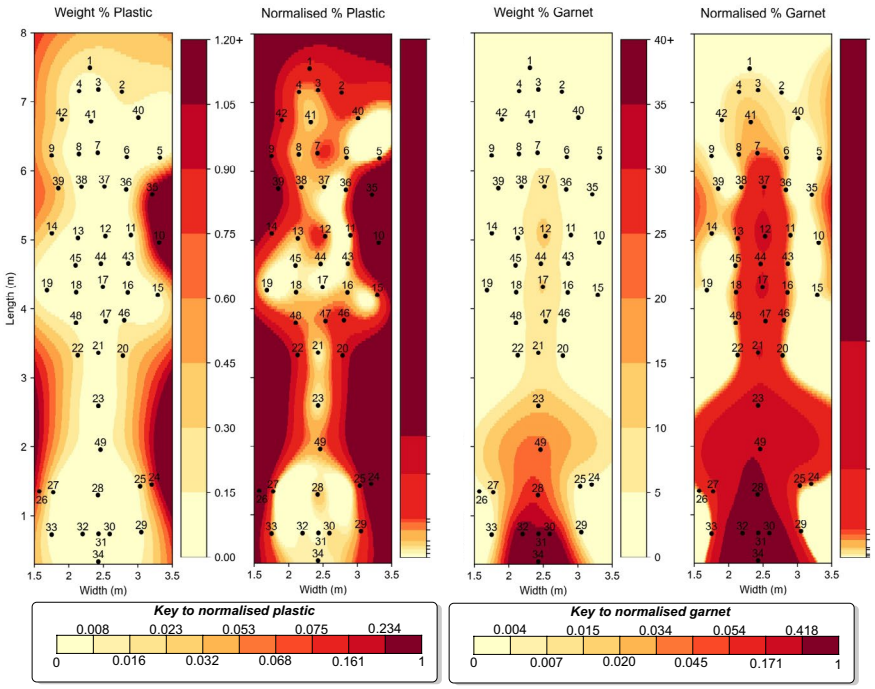

FIGURE 8 Grain-type interpolation maps of both raw and normalised values. Note different scale bar for each grain type. Normalised graphs use a percentile classification, with each class comprising 10% of values

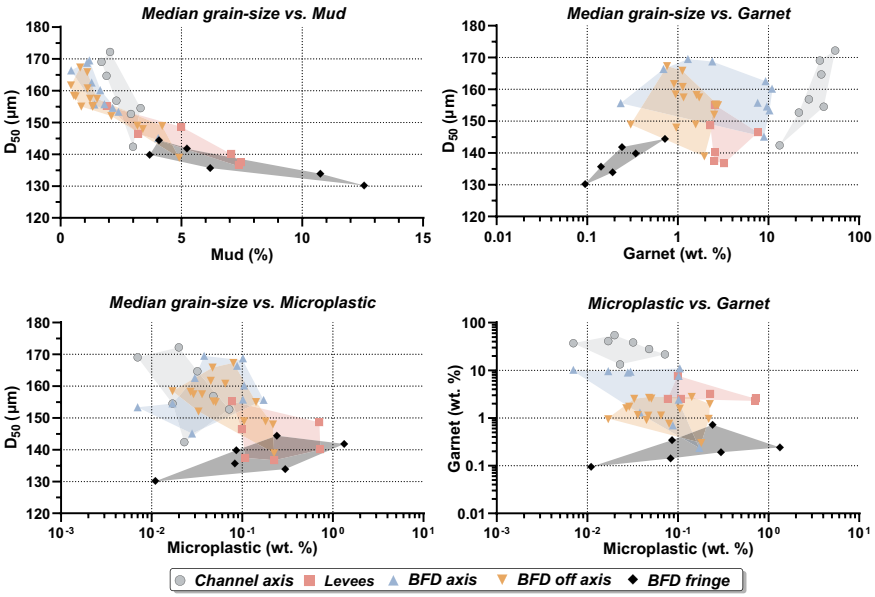

FIGURE 9 Cross-plots comparing the textural properties and composition of sample locations from sub-environments in the flow deposit. Coloured polygons were qualitatively drawn to illustrate the area each sub-environment occupies

172 µm, was recorded at the most proximal sampled position in the channel, S34 (Figure 10). The D_{50} in the channel axis decreases down-dip to 142 µm at S23 (Figure 10), probably due to the decreasing abundance of the slightly coarser-grained garnet with respect to sand. Grain size decreased laterally from the channel axis to the channel-levees (Figures 9 and 12). For example, S26 in the channel axis had a D_{50} of 157 µm, which decreased laterally to 147 and 149 µm in the levee at S27 and S28, decreases of 7% and 5%, respectively (Figure 10).

Down-dip of the channel mouth there was a general down-dip coarsening in axial BFD positions from 155 µm at S21 to 170 µm at S41 (an increase of 10%; Figures 10 and 12), the coarsest grain size recorded in the BFD. However, this coarsening is non-linear throughout the transect. There is a fining from 156 µm at S47 to 145 µm at S44, and subsequent coarsening to 160 µm at S12 (Figure 10). This coarsening-to-fining trend corresponds to the anonymously thin zone 40 cm down-dip of the channel mouth (Figures 5, 10 and 12). The D_{50} decreases down-dip of S41 to 155 µm at the most distal sampled position, S01 (Figures 10 and 12).

Median grain size also varied laterally in the BFD, the D_{50} was 140 and 134 µm at S05 and S09, the right and left lateral BFD fringe with respect to flow direction, respectively (Figure 10). In contrast, the D_{50} of the equivalent off-axis positions was 162 and 166 µm at S06 and S08, respectively

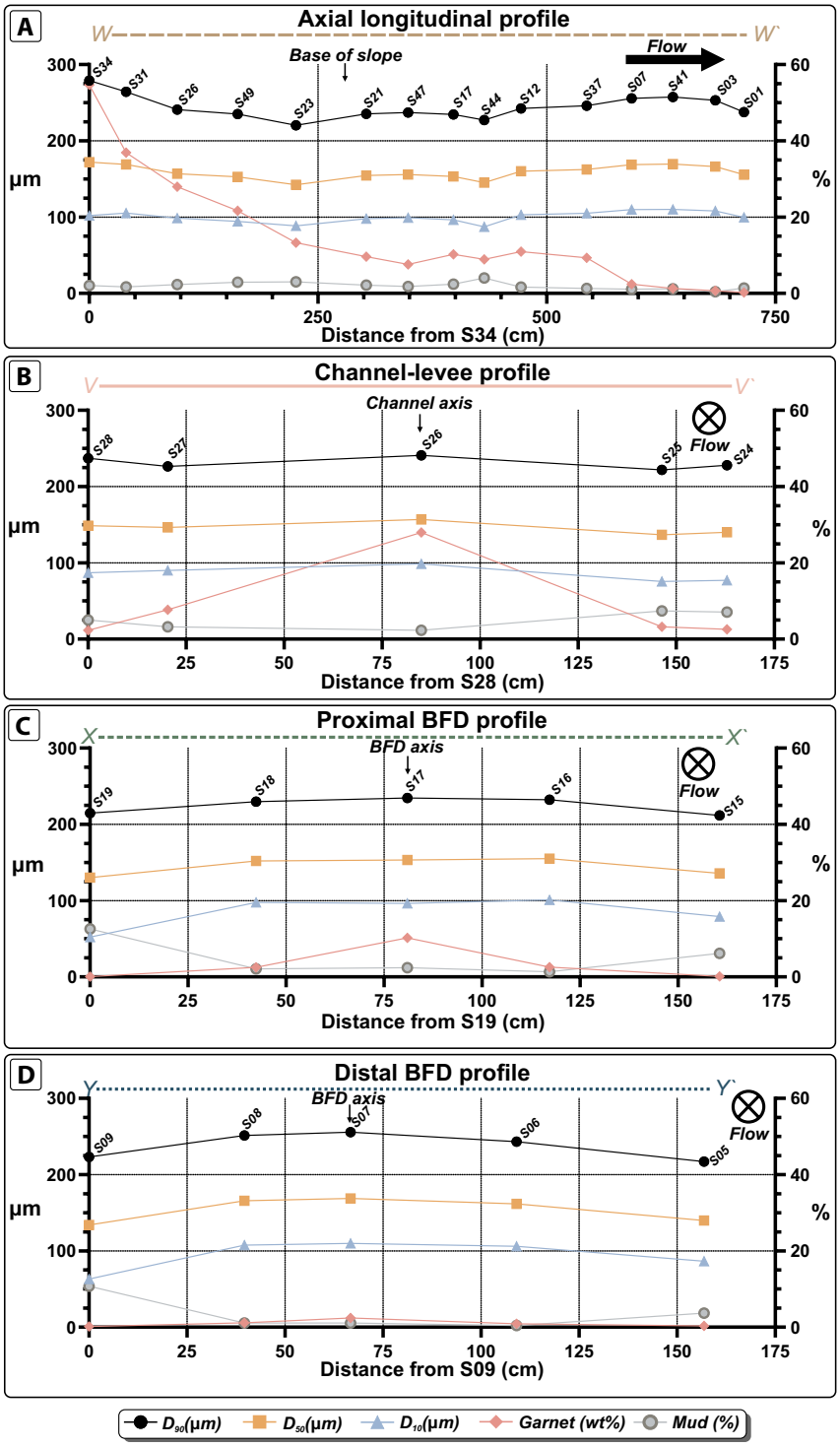

FIGURE 10 Graphs of longitudinal and lateral sample grain size and grain-type distribution in the flow deposit. (A) Depositional dip profile from most proximal axial sample to the most distal axial sample. (B) Across strike profile of the channel fill and levees. (C) Across strike profile of the proximal BFD deposit. (D) Across strike profile of the distal BFD deposit. Profile lines are located on Figure 2

(Figure 10); and 169 μm at axial position S07, 21% and 27% coarser than S05 and S09, respectively (Figure 10).

3.5.2 | 90th Percentile grain size distribution (D_{90})

Similar trends were recorded in the D_{90} of grain size measurements, which ranged from upper fine sand to lower medium sand on the Udden-Wentworth scale (Udden, 1914; Wentworth, 1922). The coarsest D_{90}, 279 μm was recorded in channel at S34, proximal to the inlet pipe (Figure 10). The finest D_{90}, 212 μm, was recorded at S15 in the lateral BFD fringe (Figure 10).

The D_{90} decreased down-dip in the channel axis, from 279 μm at S34 to 220 μm at S23, a 21% decrease (Figures 10 and 12). The D_{90} decreased laterally from 241 μm at channel axis position S26, to 228 and 237 μm

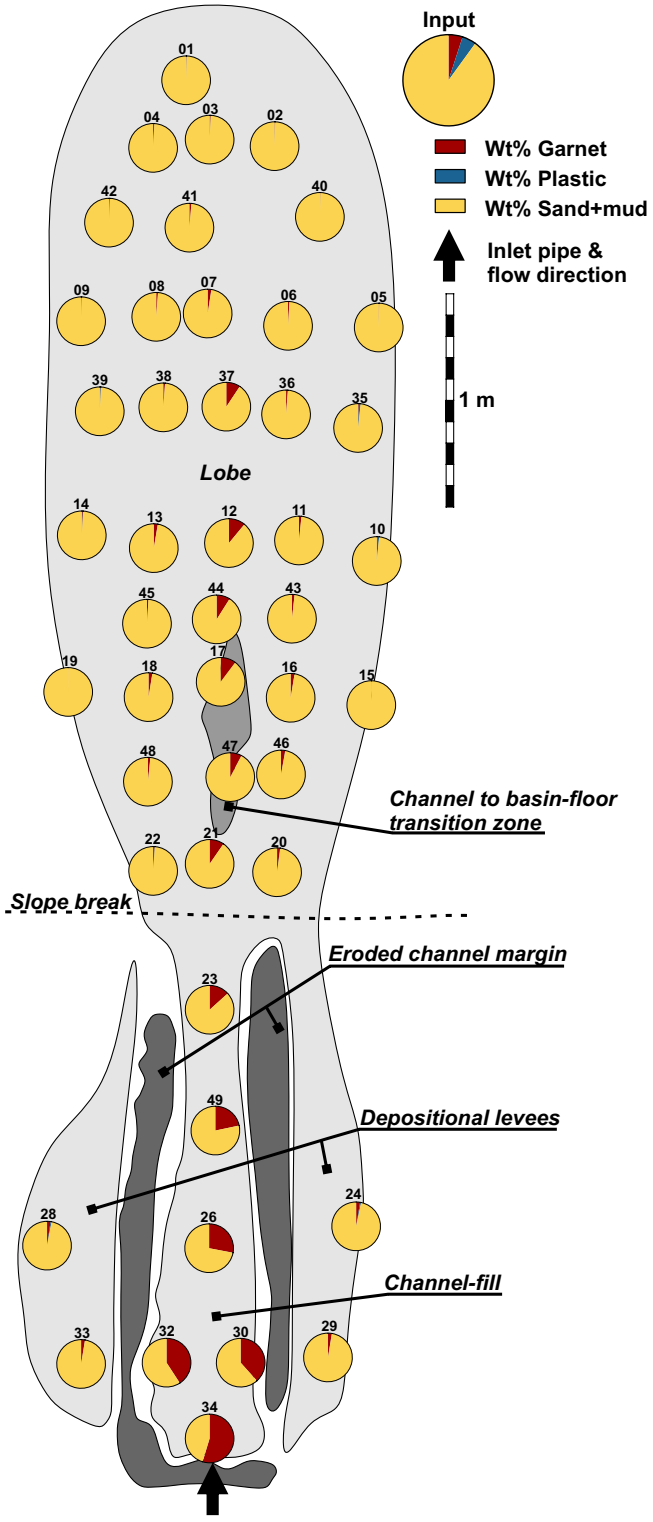

FIGURE 11 Comparison of grain-type composition of each sampled position and the original flow composition. No sample was fully representative of the original flow composition, although axial BFD positions were the most representative of the original garnet composition

at levee positions S24 and S28, decreases of 5% and 2%, respectively (Figures 10 and 12).

Immediately down-dip of the channel mouth at S21 the D_{90} was 235 μm, 15 μm coarser than the final channel axis position at S23 (220 μm; Figures 10 and 12). The D_{90} grain size generally increased down-dip from the channel mouth and CLTZ to a maximum of 257 μm at S41 in the distal BFD axis 370 and 638 cm from the break-in-slope and S34, respectively, and an increase of 9% compared to S21 (Figures 10 and 12). There is a slight fining from S47 (237 μm) to S17 (234 μm) in the CLTZ, superimposed on the overall coarsening trend observed in the BFD (Figure 10). The D_{90} grain size decreased down-dip of S41, to 253 and 238 μm at S03 and S01, respectively (Figures 10 and 12). The D_{90} decreased laterally from BFD axis positions to the BFD fringes, for example the D_{90} decreased from 255.7 μm at S07 in the BFD axis, to 217.1 and 223.1 μm at S05 and S09, the right and left lateral fringe, decreases of 15% and 13%, respectively (Figures 10 and 12).

3.5.3 | Mud distribution

Mud, here all grains <63 μm, was most abundant at BFD fringe position S19 (12.6% of grains), and least abundant at BFD off-axis position S06 (0.4% of grains; Figures 8 and 10).

In the channel and levees mud was most abundant in levee positions. For example, channel axis position S26 contained 2.3% mud (Figures 8 and 10). Mud content increased laterally to levee positions S24 and S28 by 206 and 117%, respectively (Figures 8 and 10). No strong trends were observed in channel axis positions, all samples contained <5% mud (Figure 8).

Mud was more abundant in BFD fringe positions compared to axis or off-axis positions (Figures 8–10). Lobe axis position S07 contained 1.1% mud, which increased by 1%, and decreased by 61%, at off-axis positions S08 and S06, respectively (Figures 8 and 10); mud abundance increased to BFD fringe positions S09 and S05 by 881% and 236% relative to S07, respectively (Figures 8–10). There was a slight 'cleaning' of BFD axis and off-axis sands from proximal to distal in the BFD (Figure 8). The most proximal BFD positions S20–22 contained more mud (2.2%–4.9%; Figure 8), compared to distal positions, for example S36–38 (1.1%–1.3%; Figure 8). However, the two most-distal axial positions showed an increase in mud; S03 contained 0.4% mud, which increased to 1.4% at S01 (Figures 8 and 10).

4 | DISCUSSION

4.1 | Flow processes

The spatial distribution of grain size and grain type provides insights into how flow structure and grain-support mechanisms varied across the depositional system.

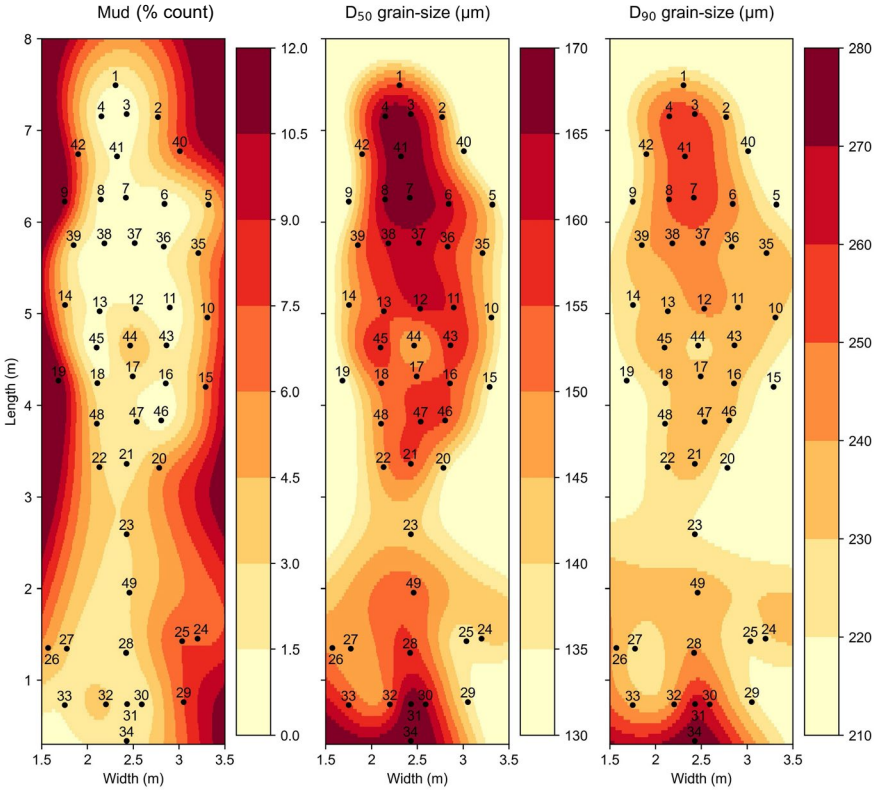

FIGURE 12 Cubic interpolation of grain size distribution in the flow deposit. Note different scales on each plot

4.2 | Channel-levee trends

Channel axis positions were coarser and contained elevated garnet concentrations compared to levee positions (Figures 9 and 10). Following Rouse (1937), although noting issues with prediction of upper-flow components raised in Eggenhuisen et al. (2020), coarser grains were probably predominantly concentrated at the base of the flow and deposited in the channel axis (Figure 13). Garnet enrichment of up to *ca* 1,000% compared to the input weight-percentage in the channel axis suggests the flow was initially far above capacity with respect to garnet (Allen, 1991; Hiscott, 1994); and that bulk scaling approaches predicting sediment transport in the flow do not capture the intricacies of a flow with grains of varying densities. In contrast, finer grains were distributed more evenly throughout the flow (i.e. were therefore more concentrated in the upper flow with respect to coarser grains) and were more able to overspill the channel on to the levees (Figure 13). These observations of coarser channel-fills and finer levees have been corroborated both experimentally, and from both modern and ancient natural systems (Altinakar et al., 1996; Eggenhuisen et al., 2020; de Leeuw et al., 2018a; Hansen et al., 2015; Jobe et al., 2017). Garnet was deposited primarily in the channel axis immediately down-dip of the inlet pipe, indicating it was not able to be held in suspension by the flow, which was strongly depositional (Figures 11 and 13). This probably resulted from flow equilibration upon exiting the inlet pipe after becoming relatively unconfined (Kneller & Buckee, 2000; Kneller & McCaffrey, 2003; Stevenson et al., 2014).

4.3 | Bypass of coarse grains

From proximal to distal in the BFD axis (i.e. S21–S01), there is an increase in grain size and associated decrease in garnet concentration (Figure 10). Similar grain size trends were observed in the experiments of de Leeuw et al. (2018b). Garnet was probably predominantly confined to the basal layers (Figure 11) due to its higher density and being transported as bedload (Alonso et al., 1991). Coarse quartz grains (i.e. $D_{90;}$ Figure 4) have a settling velocity (w_s) approximately twice that of fine garnet grains (i.e. D_{10}; Figure 4). Distal axial samples (e.g. S03) have coarser D_{50} and D_{90} values than that of the quartz sand (Figures 4 and 12) and have low concentrations of other grain types, including silt and clay (Figures 8 and 12), suggesting that coarse quartz grains preferentially bypassed proximal areas. As the flow bypassed coarser quartz grains with high w_s, but deposited finer garnet with lower w_s, it is improbable grains were deposited according to w_s axially. Therefore, it seems improbable the flow was fully turbulent and depositing according to flow competence in axial positions, and so probably had a two-phase structure (i.e. high-density turbidity current; Lowe, 1982). A potential explanation for these observations is kinetic, or kinematic, sieving in traction carpets, which enables finer grains to percolate between coarser-grains due to shearing and dilatancy (Cartigny et al., 2013; Middleton

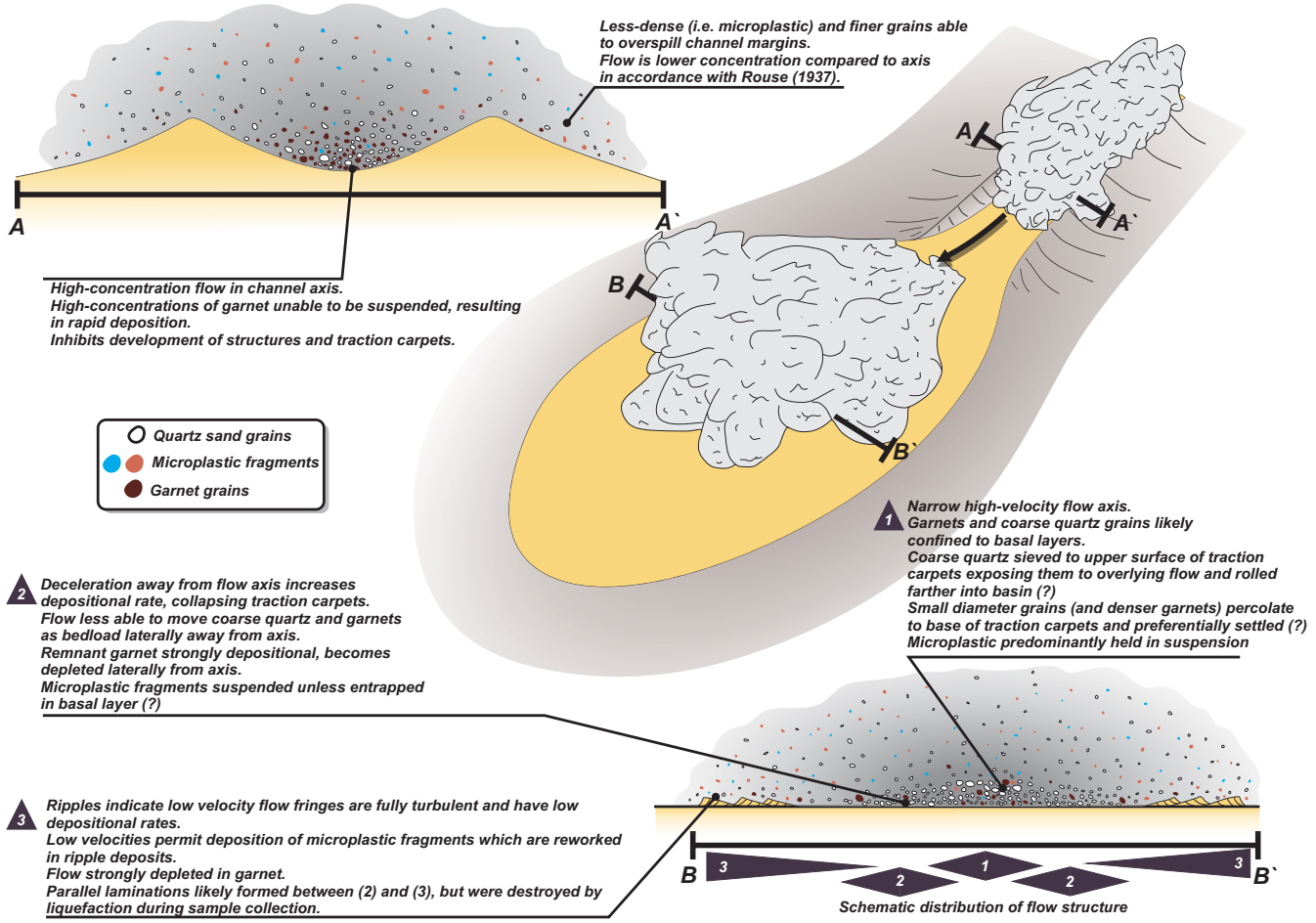

FIGURE 13 Schematic model of grain-type distribution in the flow, and how spatial variation in grain support mechanism acts to segregate grain types in the deposit

& Hampton, 1976; Sohn, 1997). This mechanism could allow finer grains to percolate downwards and be deposited at the base of the flow, whereas coarser grains of quartz were sieved to the upper surface of the traction carpets and bypassed further into the basin (Figure 13). The periodic collapse and freezing of such near-bed layers (Cartigny et al., 2013; Eggenhuisen et al., 2017; Sumner et al., 2008; Vrolijk & Southard, 1997) suggests traction carpets alone may not have transported coarse quartz grains from base-of-slope to the distal BFD. The inverse grading generated by traction carpets could have exposed the coarse quartz grains to the overriding flow, where they may have been preferentially transported (rolled) further compared to garnet due to their smaller pivot angles (Komar, 2007). Repetition of these processes could have acted to preferentially deposit finer grains (e.g. remnant garnet), whilst coarser quartz was preferentially inhibited from settling and transported downslope.

4.4 | Lateral variability

Flow deceleration inhibits kinetic sieving due to increased settling of grains causing an equal upwards flux of pore water, resulting in fine grains moving upwards rather than percolating downwards (Cartigny et al., 2013; Sumner et al., 2008). Deceleration of the flow away from the flow axis probably resulted in increased rates of settling and deposition, collapsing any traction carpets present (Figure 13). This resulted in deposition of garnet and coarser grains, which could not be suspended at low velocities, from the dense basal layer of a high-density turbidity current, inhibiting their transport away from the axis (Figure 13). The flow axis was narrow, as inferred from the limited lateral distribution of garnet; abrupt decreases in off-axis garnet content compared to axial samples suggest the flow axis had a maximum width of 80 cm (Figures 8 and 11). Similarly, the thin channel-to-BFD zone at base-of-slope (Figure 5) is interpreted to form due to flow relaxation and bypass (Pohl et al., 2019). The width of this zone suggests the flow axis had a maximum width of 50 cm. The presence of this narrow, high-velocity, flow axis provides a potential explanation for the erosion of barriers in axial positions downstream of the channel mouth in analogous experiments (Soutter et al., 2021). Fringe positions are characterised by finer-grain sizes and ripples, indicating the flow must have been fully turbulent at these positions

(Figures 5 and 12). Therefore, the flow transformed laterally from: (a) a high-density turbidity current with traction carpets in the flow axis; (b) a high-density turbidity current with strongly depositional basal layer in off-axis positions; (c) a low-density turbidity current in fringe positions (Figure 13). Parallel laminations probably developed between the flow axis and fringe positions (Baas et al., 2004), but were destroyed by liquefaction during sample collection.

4.5 | Representation of natural deposit scales

Submarine lobes and their discrete sub-environments are identified based on mapping of stacking patterns and robust facies analysis (Prélat et al., 2009). Lobe axis positions are characterised by structureless sandstones (i.e. Bouma T_a) deposited from high-density turbidity currents with subordinate structured sandstones (Prélat et al., 2009). Lobe off-axis positions are characterised by structured (typically planar laminated; i.e. Bouma T_b) sandstones, with minor structureless sandstones (Prélat et al., 2009). Lateral lobe fringes are dominated by structured (typically rippled; i.e. Bouma T_c) sandstones deposited from low-density turbidity currents (Spychala et al., 2017). The frontal fringes of lobes often, but not always, contain hybrid beds (Spychala et al., 2017). No flow transformation was observed in this study, so frontal fringes are not explicitly discussed.

In the single flow experiment described here, axial BFD's produced from a high-density turbidity current are probably most representative of lobe axis positions. Ripple laminated deposits of the BFD fringe are most representative of lobe fringe deposits. BFD off-axis deposits are probably most representative of lobe off-axis deposits as the flow decelerated and became more-dilute, representing the transition from high-density to low-density turbidity current (Talling et al., 2012).

4.6 | Implications for submarine fan architecture

Submarine lobe deposits are traditionally considered to thin and fine radially away from a locus (channel mouth) due to lateral flow spreading and dissipation of energy (Luthi, 1981). However, recent studies have documented strong spatial and architectural heterogeneities in modern and ancient lobe deposits (Dodd et al., 2019; Klaucke et al., 2004; Spychala et al., 2017; Twichell et al., 1992).

The narrow and strongly directional area of high garnet concentrations indicates the flow axis was narrow (<80 cm) and aligned with flow direction immediately down-dip of the channel (Figure 13). A similar strong axial trend was observed by Alexander et al. (2008) who documented relatively coarse-grained axial ridges down-dip of channel mouths of physical experiments. These observations from individual flows may provide insight into the development of finger-like geometries observed in lobes from numerical modelling, outcrop and subsurface data (Dodd et al., 2019; Groenenberg et al., 2010; Hansen et al., 2019; Klaucke et al., 2004; Twichell et al., 1992). Distributary channels developed in lobes, which feed some lobe fingers (Twichell et al., 1992), may develop due to self-confinement resulting from lateral flow relaxation (Pohl et al., 2019). Similarly, lobes can show lateral variability in facies and degree of amalgamation, forming high-amalgamation-zones, flanked by less-amalgamated structureless sandstones (Hodgson et al., 2006; Johnson et al., 2001; Prélat et al., 2009). At a lobe scale, these zones of high-amalgamation may be formed by the lateral switching of successive strongly axial flows such as observed in this experiment. Alexander et al. (2008) showed that slope gradient was a primary control on the development of a lateral ridge with flows able to maintain forward momentum upon exiting the channel. Similarly, Pohl et al. (2020a) document that the slope gradient is a stronger control on sediment bypass and depositional patterns at break-of-slope compared to basin floor gradient (see also: Spychala et al., 2020). Therefore, systems with steeper channel gradients, at least immediately up-dip of lobes, may be more probable to develop finger-like geometries due to focused axial flow components. Lobe deposits are also commonly considered to fine both laterally and longitudinally due to the higher settling velocities of coarse grains. However, recent studies have documented examples of downstream coarsening and stepwise fining patterns (Bell et al., 2018a; Pohl et al., 2017; Spychala et al., 2021). Strongly axial flows in which coarser grains are inhibited from settling compared to finer grains due to the effects of drag may provide a mechanism to bypass coarse grains distally into the basin (Figure 13).

4.7 | Autogenic signal shredding in deep-water systems

Autogenic modulation of signal preservation is comparatively well-studied in terrestrial and shallow-marine environments compared to submarine fans (Capaldi et al., 2019; Covault et al., 2007; Garzanti et al., 2015; Jackson et al., 2019). Here, a known composition of mixed grain types was diluted at the scale of a single turbidity current (Figure 11). No sample was fully representative of the original flow composition, and the composition of samples varied both laterally and longitudinally (Figure 11). Whilst submarine fans capture sediment from the full catchment area which can be used to interpret bulk signal changes or subsets thereof (Blum et al., 2018; Fildani et al., 2018b; Mason et al., 2019; see

also DeGraaff-Surpless et al., 2003), these data suggest any such mineralogical signal in a deep-water system is probably fractionated in response to spatially variable depositional processes. Such effects probably further exacerbate signal shredding processes in terrestrial and shallow marine parts of the system (Sickmann et al., 2016).

As mineral composition is commonly used to decipher provenance, age and palaeoenvironmental signals (i.e. changing compositions), understanding how a compositional signal is preserved at the scale of a single flow has implications for sampling strategies and interpretation of data (Figure 14). Environmental signals are often considered using numerous events or through time (Romans et al., 2016). Therefore, the dilution of an individual flow modelled here may not represent a signal sensu *stricto*. However, heavy minerals have been shown to be fractionated by spatial changes in flow processes at the bedform scale (Ibañez-Mejia et al., 2018); and individual flow deposits of discrete depositional processes make up larger scale bodies (Prélat et al., 2009). Therefore, the spatial fractionation of grain types in sediment gravity flows and their deposits, and how these deposits stack, are likely to exert a strong control on how environmental signals are preserved and realised in deep-water environments. Taking submarine lobes as an example, compensational stacking patterns mean that different lobe sub-environments can be stacked in a vertical section (Figure 14; Prélat et al., 2009). In limited or 2D exposures where genetically linked sub-environments are not exposed this could result in samples being collected from different sub-environments in which sediment was deposited from discrete depositional processes (Figure 14). Given the strong axial garnet-rich trend described here (Figures 8 and 11), an autogenic vertical transition from lobe fringe to lobe axis (i.e. deposition from low-concentration and high-concentration turbidity currents, respectively) due to compensational stacking will exhibit a marked increase in heavy minerals and may imply a change in signal or provenance from mineralogical data (Figure 14). These data demonstrate that palaeogeographic knowledge and robust facies analysis of a system is fundamental to sampling strategies and sound interpretation of mineralogical data. Similarly, samples from discrete sub-environments can suggest different source terranes from QFL (quartz, feldspar, lithic fragments) ternary diagrams (Ragusa & Kindler, 2018), and greater concentrations of heavy minerals in channel axis positions compared to overbank deposits have been

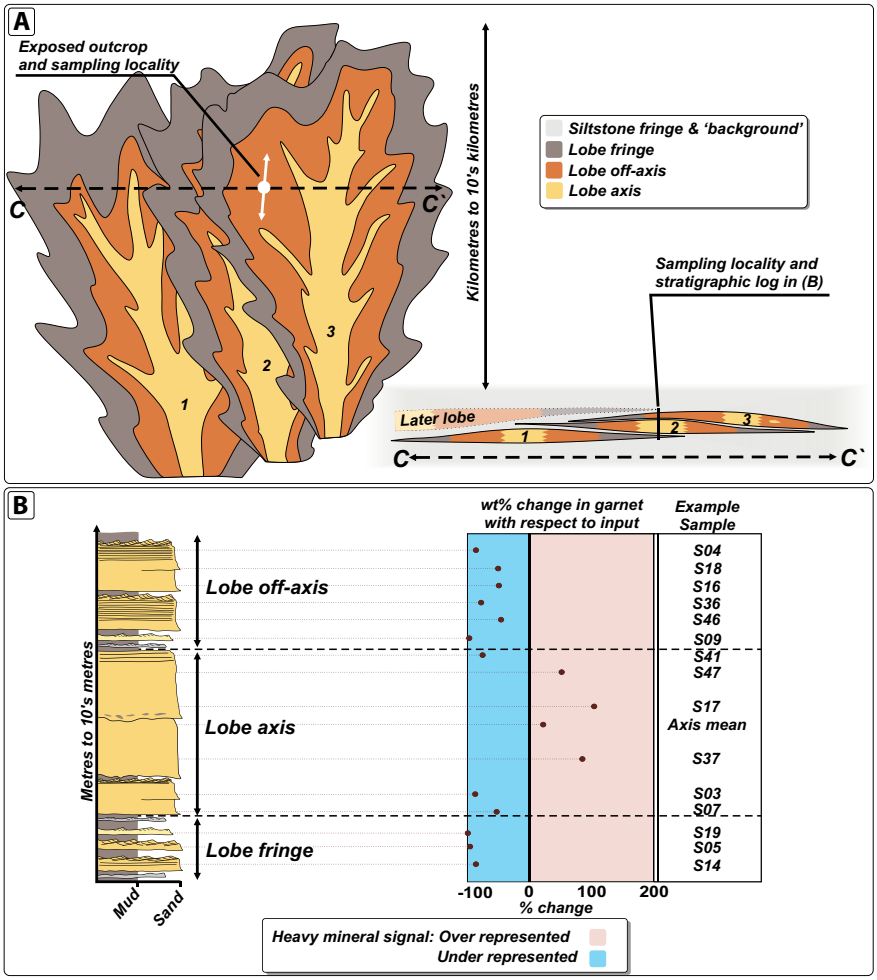

FIGURE 14 Schematic depiction of how autogenic flow-scale signals could be compounded by autogenic compensational stacking of successive lobes. (A) Example of compensationally stacked lobes in plan and cross-sectional views. The limited exposure of many ancient systems compared to the whole depositional system is also illustrated. (B) Schematic log of the position in (A). Heavy minerals are probably over-represented in lobe axis positions with respect to both original flow composition, and fringe and off-axis positions. Heavy minerals in off-axis positions are probably under-represented with respect to original flow composition and axis positions but over-represented with respect to fringe positions. Heavy minerals in lobe fringe positions are probably under-represented with respect to original flow compositions and other lobe sub-environments. Data points are from samples of equivalent positions in the experiment

observed in modern systems (Andò et al., 2019). Burgess et al. (2019) suggested that sediment supply signals are best preserved in 'mid-fan' areas. Here, the heavy mineral signal is best preserved in BFD axis positions, although the low-density microplastics are poorly represented in these positions (Figure 11).

Collecting samples of comparable grain size is sometimes used to minimise these errors (Bateman & Catt, 2007; Caja et al., 2010; Garzanti et al., 2009; Ragusa & Kindler, 2018). However, here sample composition varied markedly between samples which were both within the same grain size class and closely spaced (Figures 8, 11 and 12). This shows that in turbidite deposits the sub-environment of deposition, and depositional processes, are strong controls on mineral distribution (Figure 13). This reinforces the necessity of well-constrained stratigraphic frameworks prior to sample collection, particularly in systems with narrow grain size ranges. In natural systems with wider grain size populations of heavy minerals such an effect may be limited whereby heavy minerals are deposited with lighter grains of similar hydraulic equivalence (Garzanti et al., 2008). Here, for example, if added to the flow, silt-sized garnet may have been transportable by the flow away from the axis, enabling its concentration in the BFD fringes. However, heavy minerals can sometimes form narrow grain size classes. For instance, detrital zircons can sometimes form populations of discrete grain sizes and ages (Lawrence et al., 2011). These zircons can then be hydrodynamically fractionated during sediment transport according to their grain size (Lawrence et al., 2011). These experiments suggest zircons probably show a strong axial trend in sediment gravity flow deposits, and that coarser zircon populations are probably distributed in axial, and distal axial positions, and depleted in off-axis and marginal positions (Figure 14).

4.8 | Insights into microplastic deposition in deep-water systems

Microplastics are ubiquitous on the sea floor (Harris, 2020; Kane et al., 2020; Martin et al., 2017; Sanchez-Vidal et al., 2018; Thompson et al., 2004; Woodall et al., 2014). However, the processes transporting them to the deep oceans, and how they are spatially distributed are poorly understood (see Kane & Clare, 2019). Similarly, the diverse range of sea floor environments are sparsely sampled for microplastics (see discussion in Kane & Clare, 2019).

4.9 | Distribution and potential implications

Here a deep-water depositional system consisting of a channel, levees and a BFD were physically modelled in three dimensions. The highest microplastic fragment concentrations were recorded in levees and BFD fringe positions, whilst channel axis and BFD axis deposits contained the lowest concentrations (Figure 15). Lobe fringe positions contained the highest recorded microplastic fragment concentrations (Figure 15). Lobe fringe environments are typically areas with high biodiversity of burrowing organisms (Crimes, 1977; Heard & Pickering, 2008; Tunis & Uchman, 1996; Uchman et al., 2004). Consequently, microplastic fragments in these environments are probably readily entrained into the marine organism food chain (Courtene-Jones et al., 2017; Graham & Thompson, 2009; Näkki et al., 2017).

Given their comparable low densities some authors have suggested microplastic fragments accumulate in similar environments to particulate organic carbon (POC) (Haave et al., 2019; Maes et al., 2018; Vianello et al., 2013), although other studies note no correlation between the two (Courtene-Jones et al., 2020; Ling et al., 2017; Ronda et al., 2019). However, none of these studies document this relationship in sediment gravity flow deposits. Organic matter measured in natural sediment gravity flow deposits is often concentrated in structured (i.e. laminated or rippled) very-fine to fine sands and sandstones (Hage et al., 2020; Saller et al., 2006), typically deposited in lobe off-axis and fringe environments (Bell, et al., 2018b; Grundvåg et al., 2014; Mutti, 1977; Prélat et al., 2009). This relationship can also be inferred from elevated bioturbation in these environments (Heard & Pickering, 2008), suggesting an abundance of food (i.e. POC). Here, microplastic fragment concentrations were elevated in BFD fringe positions, suggesting POC and microplastic fragments may occupy similar depositional environments in submarine fans where high levels of bioturbation resulting from abundant POC, and availability of microplastic, may promote uptake to the food web.

Strong variability in microplastic fragment concentration was recorded in the BFD fringe; S10 and S19 contained 1.34 and 0.01 wt%, respectively (Figure 7). Qualitative observations of current ripples suggest that microplastics are strongly partitioned into the lee slopes of ripples and are relatively depleted on stoss sides (Figure 15). This suggests microplastic fragments were more-easily mobilized on the stoss slopes, and cascaded down the lee slope, or were readily incorporated into the zone of flow separation downflow of the ripple (Figure 15). As such, fringe samples with elevated microplastic concentrations may contain more lee-slope deposits, whereas microplastic-poor fringe samples may have predominantly sampled from stoss-slope deposits. While this relationship is not quantified here, this observation of highly localised microplastic segregation in bedforms may explain variability in microplastic concentrations recorded in the BFD fringe (e.g. Figure 7) and warrants future research into the behaviour of microplastics during bedform development.

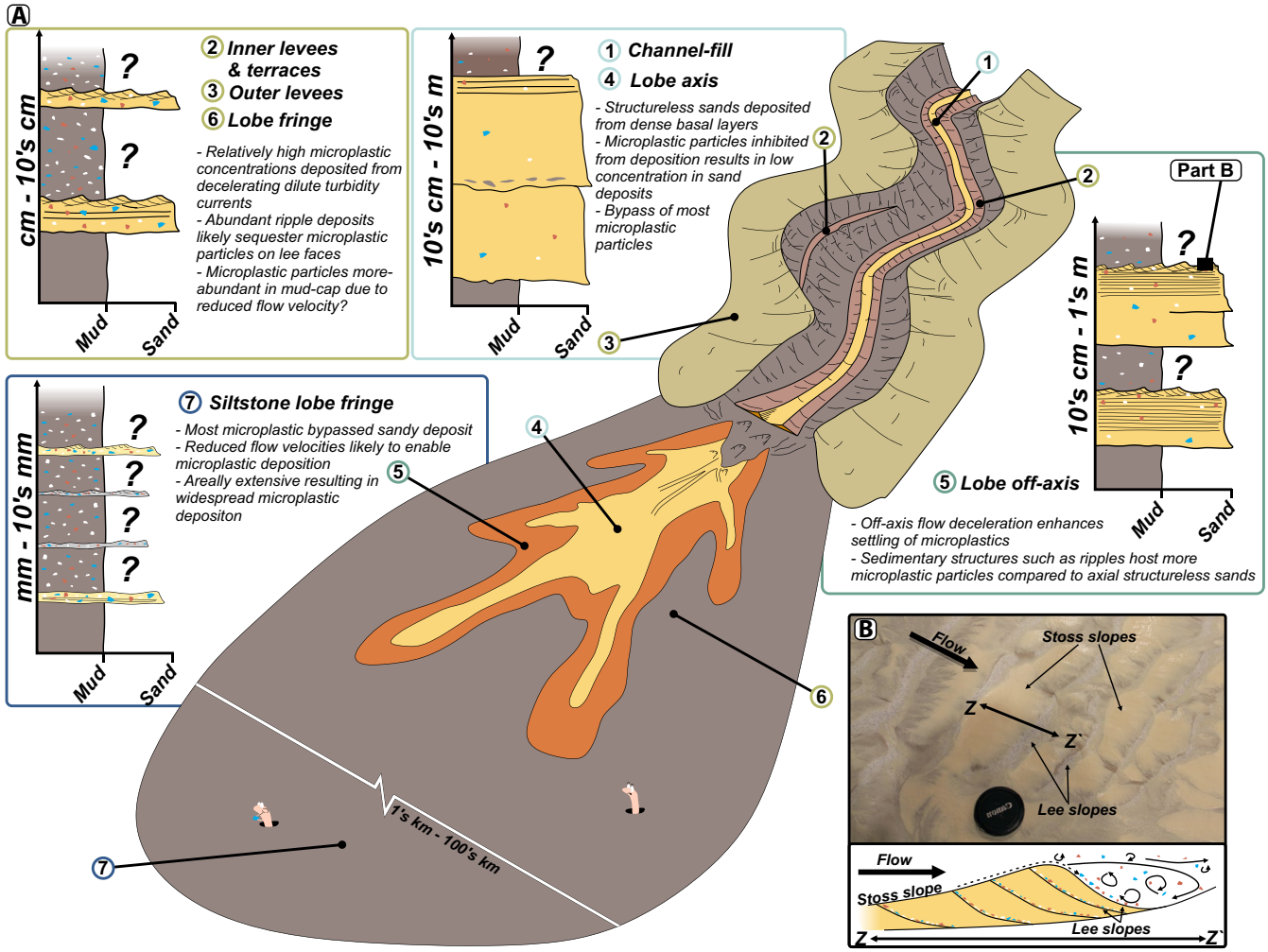

FIGURE 15 Potential implications of observed microplastic fragment distribution. (A) Predictive model of microplastic fragment distribution in deep-water sands. Axis and off-axis positions are strongly depleted in microplastic fragments which bypass to lobe fringe positions. However, even the sandy deposits in fringe positions are depleted compared to original flow composition. This suggests that microplastic fragments are likely probably strongly fractionated into mudstone caps (i.e. Bouma, 1962 T_e division), or bypass to the siltstone fringe, sensu Spychala et al. (2020), and are spread over vast expanses of the sea floor. As mudstone caps were not studied, this unknown is represented by question marks. Not to scale. (B) Top: Photograph of microplastics in ripple deposits and schematic model showing microplastic particle behaviour and concentration in ripple bedform development. Note localised microplastic abundance, and comparative absence, on the lee and stoss slopes of ripples, respectively

4.10 | The case of the missing microplastic

The flow contained a known input of 5.00 wt% microplastic fragments (Figure 11). In contrast, the highest recorded microplastic particle concentration was 1.34 wt% in the BFD fringe (Figures 8, 10 and 11), and most other sampled positions contained one to two orders of magnitude less microplastic (Figure 9). This suggests the sandy deposits of sediment gravity flows are not the major sink of microplastic fragments in the deep oceans (Figure 15). The question then becomes: Where was the microplastic stored? Three probable explanations are proposed: First, microplastics were held in suspension and bypassed the sand-prone parts of the BFD to the siltstone-prone fringe (Figure 15) (sensu Spychala et al. 2020). Spychala et al. (2020) document a siltstone-prone fringe which extends at least 270% further than the sand-prone part of the deposit in similar experimental sediment gravity flow deposits; Boulesteix et al. (2020) show siltstone-prone parts of lobes extending at least 18.5 km beyond the sand pinchout; and Stow et al. (1990) recognised finer-grained turbidites in the Bengal Fan which had travelled at least 2,500 km. If microplastics do bypass the sand-prone parts of lobes *en-masse* these examples suggest they are probably deposited over vast areas of the sea floor adjacent to continental margins, where they may also be reworked and re-concentrated by bottom currents (Kane et al., 2020). The second potential explanation for the observed microplastic distribution is that microplastic fragments are strongly partitioned into the tail of the flows and are therefore deposited in finer-grained turbidite caps associated with each bed (Figure 15). This cap

was not sampled in this study, and the flume tank was enclosed preventing the flow from achieving its natural runout distance, as such these first two models cannot be differentiated. In which case the upper divisions of turbidite beds would be most enriched in microplastics. Therefore, studies taking only surface samples of the sea floor may predict elevated microplastic fluxes compared to the full bed and flow. And thirdly, that microplastic particles are strongly fractionated into the lee slopes of ripples, which were not explicitly sampled in this study. However, the concentrations probably required mean this mechanism is not inferred to have been a primary sink in the experiment.

5 | CONCLUSIONS

The sandy deposit of an experimental sediment gravity flow containing a sediment load of quartz sand (2.65 g/cm^3), silt (2.65 g/cm^3), kaolinite (2.60 g/cm^3), garnet (3.90 g/cm^3) and microplastic fragments (1.50 g/cm^3) was sampled to investigate spatial trends in texture and composition. Grain size and grain-type analysis of spatially constrained samples tied to specific depositional environments reveal that:

1. The BFD showed a strongly axial concentration of garnet which decreased gradually downstream, whilst sample grain size increased, suggesting grains were not deposited according to their settling velocity. This is interpreted as the flow having a narrow high-velocity core in which remnant finer grains of garnet were trapped and settled at the bases of traction carpets. In contrast, coarser quartz grains may have been sieved to the upper surface traction carpets, enabling their transport farther into the basin.
2. The observed strongly axial deposit challenges traditional models of the radial spreading of gravity flows on smooth open slopes, with deposits thinning and fining away from an apex. The findings provide insight into the linear directionality observed in natural systems, such as finger-like geometries and isolated amalgamated zones.
3. A known input composition of mixed grain types was autogenically diluted by spatially variable depositional processes. No sample was fully representative of the original flow composition, and the composition of samples varied both laterally and longitudinally. These results predict a strong axial trend in heavy mineral composition in deposits of unconfined turbidity currents with dense basal layers. Autogenic (compensational) stacking of successive submarine lobes consisting of axial followed by fringe facies could therefore show substantially different compositions and counts in heavy minerals; translating composition dilution at the scale of a flow to signal dilution at the scale of a lobe or lobe complex. These data demonstrate that palaeogeographic knowledge of a system may be fundamental to sampling strategies and sound interpretation of mineralogical data from submarine fans.
4. Sample composition varied strongly between samples which were both within the same grain size class and closely spaced, indicating depositional processes act to segregate grain types even over relatively short distances. This advocates for caution when employing grain size-based sampling methods, particularly in systems with narrow grain size ranges as competence-controlled deposits (i.e. planar or ripple laminated) probably host substantially lower concentrations of heavy minerals compared to capacity limited deposits (e.g. structureless sandstones).
5. Microplastic fragments were most concentrated in the levees of the channel and the fringes of the BFD. These environments are typically amongst the most bioturbated environments of submarine fans, potentially enabling ready entrainment of microplastics into the food web.
6. All samples were depleted in microplastic (maximum of 1.34 wt%) with respect to original flow composition (5.00 wt%) suggesting that microplastic fragments are liable to either bypass the sandy parts of submarine fans and be spread over vast areas or are concentrated in the mud caps of flow deposits, and therefore prone to consumption by benthic biota.

ACKNOWLEDGMENTS

The authors are grateful to the European Plate Observing System for funding this work through a Transnational Access grant. Utrecht University is thanked for hosting the experiments. They thank Florian Pohl and Mike Tilston for technical assistance and advice. Tom Bishop is thanked for assisting with grain size analysis. They are grateful to Merren Jones for providing laboratory access to complete the settling analysis. They thank Emmanuel Roquette and James Lovell-Kennedy for assistance with density separation. They are grateful to reviewers Chris Stevenson and Zachary Sickmann for their constructive comments which refined this manuscript.

AUTHOR CONTRIBUTIONS

DB, ES, ZC, IK and JE devised the study. All authors performed the flume tank experiment and assisted in the associated planning and logistics. DB, ZC, ES and RF performed grain size and grain-type analysis. DB took the lead in writing the manuscript. All authors provided critical feedback that helped shape the manuscript.

DATA AVAILABILITY STATEMENT

The data that support the findings of this study are available in the supplementary material of this article.

ORCID

Daniel Bell https://orcid.org/0000-0001-5939-0283
Ross A. Ferguson https://orcid.org/0000-0001-8089-825X
Yvonne T. Spychala https://orcid.org/0000-0002-3896-9234
Joris T. Eggenhuisen https://orcid.org/0000-0002-7389-9665

REFERENCES

Alexander, J., McLelland, S.J., Gray, T.E., Vincent, C.E., Leeder, M.R. & Ellett, S. (2008) Laboratory sustained turbidity currents form elongate ridges at channel mouths. *Sedimentology*, *55*, 845–868.

Alexander, J. & Morris, S. (1994) Observations on experimental, non-channelized, high-concentration turbidity currents and variations in deposits around obstacles. *Journal of Sedimentary Research*, *10*, 899–909.

Allen, J.R.L. (1991) The Bouma division A and the possible duration of turbidity currents. *Journal of Sedimentary Research*, *61*, 291–295.

Alonso, M., Satoh, M. & Miyanami, K. (1991) Optimum combination of size ratio, density ratio and concentration to minimize free surface segregation. *Powder Technology*, *68*, 145–152.

Altinakar, M.S., Graf, W.H. & Hopfinger, E.J. (1996) Flow structure in turbidity currents. *Journal of Hydraulic Research*, *34*, 713–718.

Andò, S., Aharonovich, S., Hahn, A., George, S.C., Clift, P.D. & Garzanti, E. (2019) Integrating heavy-mineral, geochemical and biomarker analyses of Plio-Pleistocene sandy and silty turbidites: a novel approach for provenance studies (Indus Fan, IODP Expedition 355). *Geological Magazine*, *157*, 929–938.

Baas, J.H., Best, J.L. & Peakall, J. (2011) Depositional processes, bedform development and hybrid bed formation in rapidly decelerated cohesive (mud-sand) sediment flows. *Sedimentology*, *58*, 1953–1987.

Baas, J.H., Best, J.L., Peakall, J. & Wang, M. (2009) A phase diagram for turbulent, transitional, and laminar clay suspension flows. *Journal of Sedimentary Research*, *79*, 162–183.

Baas, J.H., Van Kesteren, W. & Postma, G. (2004) Deposits of depletive high-density turbidity currents: a flume analogue of bed geometry, structure and texture. *Sedimentology*, *51*, 1053–1088.

Baker, M.L., Baas, J.H., Malarkey, J., Jacinto, R.S., Craig, M.J., Kane, I.A. & Barker, S. (2017) The effect of clay type on the properties of cohesive sediment gravity flows and their deposits. *Journal of Sedimentary Research*, *87*, 1176–1195.

Bateman, R.M. & Catt, J.A. (2007) Provenance and palaeoenvironmental interpretation of superficial deposits, with particular reference to post-depositional modification of heavy mineral assemblages. In: Mange, M.A. & D.T.B.T.-D. in S. Wright (Eds.) *Heavy minerals in use*, vol. 8. Amsterdam: Elsevier, pp. 151–188.

Baudin, F., Disnar, J.-R., Martinez, P. & Dennielou, B. (2010) Distribution of the organic matter in the channel-levees systems of the Congo mud-rich deep-sea fan (West Africa). Implication for deep offshore petroleum source rocks and global carbon cycle. *Marine and Petroleum Geology*, *27*, 995–1010.

Bell, D., Kane, I.A., Pontén, A.S.M., Flint, S.S., Hodgson, D.M. & Barrett, B.J. (2018a) Spatial variability in depositional reservoir quality of deep-water channel-fill and lobe deposits. *Marine and Petroleum Geology*, *98*, 97–115.

Bell, D., Stevenson, C.J., Kane, I.A., Hodgson, D.M. & Poyatos-Moré, M. (2018b) Topographic controls on the development of contemporaneous but contrasting basin-floor depositional architectures. *Journal of Sedimentary Research*, *88*, 1166–1189.

Blum, M., Rogers, K., Gleason, J., Najman, Y., Cruz, J. & Fox, L. (2018) Allogenic and autogenic signals in the stratigraphic record of the Deep-Sea Bengal Fan. *Scientific Reports*, *8*, 7973.

Boulesteix, K., Poyatos-Moré, M., Hodgson, D.M., Flint, S.S. & Taylor, K.G. (2020) Fringe or background: characterizing deep-water mudstones beyond the basin-floor fan sandstone pinchout. *Journal of Sedimentary Research*, *90*, 1678–1705.

Bouma, A.H. (1962) *Sedimentology of some flysch deposits: a graphic approach to facies interpretation*. Amsterdam: Elsevier, 168 pp.

Burgess, P.M., Masiero, I., Toby, S.C. & Duller, R.A. (2019) A big fan of signals? Exploring autogenic and allogenic process and product in a numerical stratigraphic forward model of submarine-fan development. *Journal of Sedimentary Research*, *89*, 1–12.

Caja, M.A., Marfil, R., Garcia, D., Remacha, E., Morad, S., Mansurbeg, H., Amorosi, A., Martínez-Calvo, C. & Lahoz-Beltrá, R. (2010) Provenance of siliciclastic and hybrid turbiditic arenites of the Eocene Hecho Group, Spanish Pyrenees: implications for the tectonic evolution of a foreland basin. *Basin Research*, *22*, 157–180.

Capaldi, T.N., George, S.W.M., Hirtz, J.A., Horton, B.K. & Stockli, D.F. (2019) Fluvial and eolian sediment mixing during changing climate conditions recorded in Holocene Andean foreland deposits from Argentina (31–33°S). *Frontiers in Earth Science*, *7*, 298.

Cartigny, M.J.B., Eggenhuisen, J.T., Hansen, E.W.M. & Postma, G. (2013) Concentration-dependent flow stratification in experimental high-density turbidity currents and their relevance to turbidite facies models. *Journal of Sedimentary Research*, *83*, 1046–1064.

Choux, C.M. & Druitt, T.H. (2002) Analogue study of particle segregation in pyroclastic density currents, with implications for the emplacement mechanisms of large ignimbrites. *Sedimentology*, *49*, 907–928.

Courtene-Jones, W., Quinn, B., Ewins, C., Gary, S.F. & Narayanaswamy, B.E. (2020) Microplastic accumulation in deep-sea sediments from the Rockall Trough. *Marine Pollution Bulletin*, *154*, 111092.

Courtene-Jones, W., Quinn, B., Gary, S.F., Mogg, A.O.M. & Narayanaswamy, B.E. (2017) Microplastic pollution identified in deep-sea water and ingested by benthic invertebrates in the Rockall Trough, North Atlantic Ocean. *Environmental Pollution*, *231*, 271–280.

Covault, J.A., Normark, W.R., Romans, B.W. & Graham, S.A. (2007) Highstand fans in the California borderland: the overlooked deep-water depositional systems. *Geology*, *35*, 783.

Crimes, T.P. (1977) Trace fossils of an Eocene deep-sea fan, northern Spain. In: Crimes, P.T. & Harper, J.C. (Eds.) *Trace fossils 2*. *Geological Journal Special Issue*, *9*, 71–90.

de Leeuw, J., Eggenhuisen, J.T. & Cartigny, M.J.B. (2016) Morphodynamics of submarine channel inception revealed by new experimental approach. *Nature Communications*, *7*, 1–7.

de Leeuw, J., Eggenhuisen, J.T. & Cartigny, M.J.B. (2018a) Linking submarine channel–levee facies and architecture to flow structure of turbidity currents: insights from flume tank experiments. *Sedimentology*, *65*, 931–951.

de Leeuw, J., Eggenhuisen, J.T., Spychala, Y.T., Heijnen, M.S., Am, F. & Cartigny, M.J.B. (2018b) Sediment volume and grain-size partitioning between submarine channel–Levee systems and lobes: an experimental study. *Journal of Sedimentary Research*, *88*, 777–794.

DeGraaff-Surpless, K., Mahoney, J.B., Wooden, J.L. & McWilliams, M.O. (2003) Lithofacies control in detrital zircon provenance studies: insights from the Cretaceous Methow basin, southern Canadian Cordillera. *Geological Society of America Bulletin*, *115*, 899–915.

Dickinson, W.R. & Suczek, C.A. (1979) Plate tectonics and sandstone compositions. *American Association of Petroleum Geologists Bulletin*, *63*, 2164–2182.

Dodd, T.J.H., McCarthy, D.J. & Richards, P.C. (2019) A depositional model for deep-lacustrine, partially confined, turbidite fans: early Cretaceous, North Falkland Basin. *Sedimentology*, *66*, 53–80.

Eggenhuisen, J.T., Cartigny, M.J.B. & de Leeuw, J. (2017) Physical theory for near-bed turbulent particle suspension capacity. *Earth Surface Dynamics*, *5*, 269–281.

Eggenhuisen, J.T., Tilston, M.C., de Leeuw, J., Pohl, F. & Cartigny, M.J.B. (2020) Turbulent diffusion modelling of sediment in turbidity currents: an experimental validation of the Rouse approach. *The Depositional Record*, *6*, 203–216.

Emmel, F.J. & Curray, J.R. (1983) The Bengal Submarine Fan, Northeastern Indian ocean. *Geo-Marine Letters*, *3*, 119–124.

Ferguson, R.I. & Church, M. (2004) A simple universal equation for grain settling velocity. *Journal of Sedimentary Research*, *74*, 933–937.

Ferguson, R.A., Kane, I.A., Eggenhuisen, J.T., Pohl, F., Tilston, M., Spychala, Y.T. & Brunt, R.L. (2020) Entangled external and internal controls on submarine fan evolution: an experimental perspective. *The Depositional Record*, *6*, 605–624. https://doi.org/10.1002/dep2.109

Fernandes, A.M., Buttles, J. & Mohrig, D. (2020) Flow substrate interactions in aggrading and degrading submarine channels. *Journal of Sedimentary Research*, *90*, 573–583.

Fildani, A., Clark, J., Covault, J.A., Power, B., Romans, B.W. & Aiello, I.W. (2018a) Muddy sand and sandy mud on the distal Mississippi fan: implications for lobe depositional processes. *Geosphere*, *14*, 1051–1066.

Fildani, A., Hessler, A.M., Mason, C.C., McKay, M.P. & Stockli, D.F. (2018b) Late Pleistocene glacial transitions in North America altered major river drainages, as revealed by deep-sea sediment. *Scientific Reports*, *8*, 13839.

Fontana, D., Zuffa, G.G. & Garzanti, E. (1989) The interaction of eustacy and tectonism from provenance studies of the Eocene Hecho Group Turbidite Complex (South-Central Pyrenees, Spain). *Basin Research*, *2*, 223–237.

Fuhrmann, A., Kane, I.A., Clare, M.A., Ferguson, R.A., Schomacker, E., Bonamini, E. & Contreras, F.A. (2020) Hybrid turbidite-drift channel complexes: an integrated multiscale model. *Geology*, *48*, 562–568.

Galy, V., France-Lanord, C., Beyssac, O., Faure, P., Kudrass, H. & Palhol, F. (2007) Efficient organic carbon burial in the Bengal fan sustained by the Himalayan erosional system. *Nature*, *450*, 407.

Galy, V., France-Lanord, C. & Lartiges, B. (2008) Loading and fate of particulate organic carbon from the Himalaya to the Ganga-Brahmaputra delta. *Geochimica et Cosmochimica Acta*, *72*, 1767–1787.

Garcia, M. & Parker, G. (1989) Experiments on hydraulic jumps in turbidity currents near a canyon-fan transition. *Science*, *245*, 393–396.

Garzanti, E., Andò, S. & Vezzoli, G. (2008) Settling equivalence of detrital minerals and grain-size dependence of sediment composition. *Earth and Planetary Science Letters*, *273*, 138–151.

Garzanti, E., Andò, S. & Vezzoli, G. (2009) Grain-size dependence of sediment composition and environmental bias in provenance studies. *Earth and Planetary Science Letters*, *277*, 422–432.

Garzanti, E., Andò, S., Vezzoli, G., Megid, A.A.A. & El Kammar, A. (2006) Petrology of Nile River sands (Ethiopia and Sudan): sediment budgets and erosion patterns. *Earth and Planetary Science Letters*, *252*, 327–341.

Garzanti, E., Resentini, A., Andò, S., Vezzoli, G., Pereira, A. & Vermeesch, P. (2015) Physical controls on sand composition and relative durability of detrital minerals during ultra-long distance littoral and aeolian transport (Namibia and southern Angola). *Sedimentology*, *62*, 971–996.

Graham, E.R. & Thompson, J.T. (2009) Deposit- and suspension-feeding sea cucumbers (Echinodermata) ingest plastic fragments. *Journal of Experimental Marine Biology and Ecology*, *368*, 22–29.

Groenenberg, R.M., Hodgson, D.M., Prélat, A., Luthi, S.M. & Flint, S.S. (2010) Flow-deposit interaction in submarine lobes: insights from outcrop observations and realizations of a process-based numerical model. *Journal of Sedimentary Research*, *80*, 252–267.

Grundvåg, S.A., Johannessen, E.P., Helland-Hansen, W. & Plink-Björklrklund, P. (2014) Depositional architecture and evolution of progradationally stacked lobe complexes in the Eocene Central Basin of Spitsbergen. *Sedimentology*, *61*, 535–569.

Gwiazda, R., Paull, C.K., Ussler, W. & Alexander, C.R. (2015) Evidence of modern fine-grained sediment accumulation in the Monterey Fan from measurements of the pesticide DDT and its metabolites. *Marine Geology*, *363*, 125–133.

Haave, M., Lorenz, C., Primpke, S. & Gerdts, G. (2019) Different stories told by small and large microplastics in sediment - first report of microplastic concentrations in an urban recipient in Norway. *Marine Pollution Bulletin*, *141*, 501–513.

Hage, S., Galy, V.V., Cartigny, M.J.B., Acikalin, S., Clare, M.A., Gröcke, D.R., Hilton, R.G., Hunt, J.E., Lintern, D.G., McGhee, C.A., Parsons, D.R., Stacey, C.D., Sumner, E.J. & Talling, P.J. (2020) Efficient preservation of young terrestrial organic carbon in sandy turbidity-current deposits. *Geology*, *48*, 882–887.

Hansen, L.A.S., Callow, R.H.T., Kane, I.A., Gamberi, F., Rovere, M., Cronin, B.T. & Kneller, B.C. (2015) Genesis and character of thin-bedded turbidites associated with submarine channels. *Marine and Petroleum Geology*, *67*, 852–879.

Hansen, L.A.S., Hodgson, D.M., Pontén, A., Bell, D. & Flint, S. (2019) Quantification of basin-floor fan pinchouts: examples from the Karoo Basin, South Africa. *Frontiers in Earth Science*, *7*, 12.

Harris, P.T. (2020) The fate of microplastic in marine sedimentary environments: a review and synthesis. *Marine Pollution Bulletin*, *158*, 111398.

Heard, T.G. & Pickering, K.T. (2008) Trace fossils as diagnostic indicators of deep-marine environments, Middle Eocene Ainsa-Jaca basin, Spanish Pyrenees. *Sedimentology*, *55*, 809–844.

Hiscott, R.N. (1994) Loss of capacity, not competence, as the fundamental process governing deposition from turbidity currents. *Journal of Sedimentary Research*, *64*, 209–214.

Hodgson, D.M., Flint, S.S., Hodgetts, D., Drinkwater, N.J., Johannessen, E.P. & Luthi, S.M. (2006) Stratigraphic evolution of fine-grained submarine fan systems, Tanqua Depocenter, Karoo Basin, South Africa. *Journal of Sedimentary Research*, *76*, 20–40.

Hodson, J.M. & Alexander, J. (2010) The effects of grain-density variation on turbidity currents and some implications for the deposition of carbonate turbidites. *Journal of Sedimentary Research*, *80*, 515–528.

Hussain, A., Haughton, P.D.W., Shannon, P.M., Turner, J.N., Pierce, C.S., Obradors-Latre, A., Barker, S.P. & Martinsen, O.J. (2020) High-resolution X-ray fluorescence profiling of hybrid event beds: implications for sediment gravity flow behaviour and deposit structure. *Sedimentology*, *67*, 2850–2882. https://doi.org/10.1111/sed.12722

Ibañez-Mejia, M., Pullen, A., Pepper, M., Urbani, F., Ghoshal, G. & Ibañez-Mejia, J.C. (2018) Use and abuse of detrital zircon U-Pb geochronology—a case from the Río Orinoco delta, eastern Venezuela. *Geology*, *46*, 1019–1022.

Jackson, L.J., Horton, B.K. & Vallejo, C. (2019) Detrital zircon U-Pb geochronology of modern Andean rivers in Ecuador: fingerprinting

tectonic provinces and assessing downstream propagation of provenance signals. *Geosphere*, *15*, 1943–1957.

Jobe, Z., Sylvester, Z., Pittaluga, M.B., Frascati, A., Pirmez, C., Minisini, D., Howes, N. & Cantelli, A. (2017) Facies architecture of submarine channel deposits on the western Niger Delta slope: implications for grain-size and density stratification in turbidity currents. *Journal of Geophysical Research Earth Surface*, *122*, 473–491.

Johnson, S., Flint, S., Hinds, D. & Wickens, H. (2001) Anatomy of basin floor to slope turbidite systems, Tanqua Karoo, South Africa: sedimentology, sequence stratigraphy and implications for subsurface. *Sedimentology*, *48*, 987–1023.

Kane, I.A. & Clare, M.A. (2019) Dispersion, accumulation, and the ultimate fate of microplastics in deep-marine environments: a review and future directions. *Frontiers in Earth Science*, *7*, 80.

Kane, I.A., Clare, M.A., Miramontes, E., Wogelius, R., Rothwell, J.J., Garreau, P. & Pohl, F. (2020) Seafloor microplastic hotspots controlled by deep-sea circulation. *Science*, *368*, 1140–1145.

Kane, I.A., Pontén, A.S.M., Vangdal, B., Eggenhuisen, J.T., Hodgson, D.M. & Spychala, Y.T. (2017) The stratigraphic record and processes of turbidity current transformation across deep-marine lobes. *Sedimentology*, *64*, 1236–1273.

Klaucke, I., Masson, D.G., Kenyon, N.H. & Gardner, J.V. (2004) Sedimentary processes of the lower Monterey Fan channel and channel-mouth lobe. *Marine Geology*, *206*, 181–198.

Kneller, B. & Buckee, C. (2000) The structure and fluid mechanics of turbidity currents: a review of some recent studies and their geological implications. *Sedimentology*, *47*, 62–94.

Kneller, B.C. & McCaffrey, W.D. (2003) The interpretation of vertical sequences in turbidite beds: the influence of longitudinal flow structure. *Journal of Sedimentary Research*, *73*, 706–713.

Komar, P.D. (2007) The entrainment, transport and sorting of heavy minerals by waves and currents. In: Mange, M.A. & Wright, D.T. (Eds.) *Heavy minerals in use*, vol. *58*. Amsterdam: Elsevier, pp. 3–48.

Kuenen, P.H. (1951) Properties of turbidity currents of high density. In: Hough, J.L. (Ed.) *Turbidity currents and the transportation of coarse sediments to deep water, a symposium*, vol. 2. Groningen, the Netherlands: Society of Economic Paleontologists and Mineralogists, pp. 14–33.

Kuenen, P.H. (1966) Experimental turbidite lamination in a circular flume. *The Journal of Geology*, *74*, 523–545.

Lawrence, R.L., Cox, R., Mapes, R.W. & Coleman, D.S. (2011) Hydrodynamic fractionation of zircon age populations. *Geological Society of America Bulletin*, *123*, 295–305.

Ling, S.D., Sinclair, M., Levi, C.J., Reeves, S.E. & Edgar, G.J. (2017) Ubiquity of microplastics in coastal seafloor sediments. *Marine Pollution Bulletin*, *121*, 104–110.

Lowe, D.R. (1982) Sediment gravity flows:II depositional models with special reference to the deposits of high-density turbidity currents. *Journal of Sedimentary Research*, *52*, 279–297.

Luthi, S. (1981) Experiments on non-channelized turbidity currents and their deposits. *Marine Geology*, *40*, 59–68.

Maes, T., Barry, J., Leslie, H.A., Vethaak, A.D., Nicolaus, E.E.M., Law, R.J., Lyons, B.P., Martinez, R., Harley, B. & Thain, J.E. (2018) Below the surface: twenty-five years of seafloor litter monitoring in coastal seas of North West Europe (1992–2017). *Science of the Total Environment*, *630*, 790–798.

Mani, T., Hauk, A., Walter, U. & Burkhardt-Holm, P. (2015) Microplastics profile along the Rhine River. *Scientific Reports*, *5*, 17988.

Martin, J., Lusher, A., Thompson, R.C. & Morley, A. (2017) The Deposition and accumulation of microplastics in marine sediments and bottom water from the Irish Continental Shelf. *Scientific Reports*, *7*, 10772.

Marzano, M.S. (1988) Controls on permeability for unconsolidated sands from conventional core data offshore Gulf of Mexico. *American Association of Petroleum Geologists Bulletin*, *38*, 113–120.

Mason, C.C., Fildani, A., Gerber, T., Blum, M.D., Clark, J.D. & Dykstra, M. (2017) Climatic and anthropogenic influences on sediment mixing in the Mississippi source-to-sink system using detrital zircons: late Pleistocene to recent. *Earth and Planetary Science Letters*, *466*, 70–79.

Mason, C.C., Romans, B.W., Stockli, D.F., Mapes, R.W. & Fildani, A. (2019) Detrital zircons reveal sea-level and hydroclimate controls on Amazon River to deep-sea fan sediment transfer. *Geology*, *47*, 563–567.

McLennan, S.M., McCulloch, M.T., Taylor, S.R. & Maynard, J.B. (1989) Effects of sedimentary sorting on neodymium isotopes in deep-sea turbidites. *Nature*, *337*, 547–549.

Mériaux, C.A. & Kurz-Besson, C.B. (2017) A study of gravity currents carrying polydisperse particles along a V-shaped valley. *European Journal of Mechanics – B/Fluids*, *63*, 52–65.

Middleton, G.V. (1967) Experiments on density and turbidity currents: III. Deposition of sediment. *Canadian Journal of Earth Sciences*, *4*, 475–505.

Middleton, G.V. & Hampton, M.A. (1976) Subaqueous sediment transport and deposition by sediment gravity flows. In: Stanley, D.J. & Swift, D.J.P. (Eds.) *Marine sediment transport and environment management*. New York, NY: Wiley, pp. 196–218.

Middleton, G.V. & Southard, J.B. (1984) Mechanics of sediment transport. *SEPM Short Course*, *3*, 401.

Morton, A.C. & Hallsworth, C. (1994) Identifying provenance-specific features of detrital heavy mineral assemblages in sandstones. *Sedimentary Geology*, *90*, 241–256.

Mulder, T. & Syvitski, J.P.M. (1995) Turbidity currents generated at river mouths during exceptional discharges to the world oceans. *The Journal of Geology*, *103*, 285–299.

Mutti, E. (1977) Distinctive thin-bedded turbidite facies and related depositional environments in the Eocene Hecho Group (South-central Pyrenees, Spain). *Sedimentology*, *24*, 107–131.

Näkki, P., Setälä, O. & Lehtiniemi, M. (2017) Bioturbation transports secondary microplastics to deeper layers in soft marine sediments of the northern Baltic Sea. *Marine Pollution Bulletin*, *119*, 255–261.

Norman, T.N. (1969) A method to study the distribution of heavy-mineral grain abundance in a turbidite. *Sedimentology*, *13*, 263–280.

Normark, W.R. (1970) Growth patterns of deep-sea fans. *American Association of Petroleum Geologists Bulletin*, *54*, 2170–2195.

Paull, C.K., Talling, P.J., Maier, K.L., Parsons, D., Xu, J., Caress, D.W., Gwiazda, R., Lundsten, E.M., Anderson, K., Barry, J.P., Chaffey, M., O'Reilly, T., Rosenberger, K.J., Gales, J.A., Kieft, B., McGann, M., Simmons, S.M., McCann, M., Sumner, E.J., Clare, M.A. & Cartigny, M.J. (2018) Powerful turbidity currents driven by dense basal layers. *Nature Communications*, *9*, 4114.

Pohl, F., de Leeuw, J., Eggenhuisen, J.T., Cartigny, M.J.B., Spychala, Y.T., Tilston, M.C. & Berends, N. (2017) *Downstream grain-size coarsening in proximal lobe deposits of the Karoo Basin compared with comparable flume experiments*. Houston: American Association of Petroleum Geologists Annual Convention and Exhibition.

Pohl, F., Eggenhuisen, J.T., Cartigny, M.J.B., Tilston, M.C., de Leeuw, J. & Hermidas, N. (2020a) The influence of a slope break on turbidite deposits: an experimental investigation. *Marine Geology*, *424*, 106160.

Pohl, F., Eggenhuisen, J.T., Kane, I.A. & Clare, M.A. (2020b) Transport and burial of microplastics in deep-marine sediments by turbidity currents. *Environmental Science and Technology*, *54*, 4180–4189.

Pohl, F., Eggenhuisen, J.T., Tilston, M. & Cartigny, M.J.B. (2019) New flow relaxation mechanism explains scour fields at the end of submarine channels. *Nature Communications*, *10*, 4425.

Porten, K.W., Kane, I.A., Warchol, M. & Southern, S.J. (2016) Depositional reservoir quality of deep-marine sandstones: a sedimentolgical process-based approach – an example from the Springrar Formation, North-Western Vøring Basin, Norwegian Sea. *Journal of Sedimentary Research*, *86*, 1269–1286.

Postma, G. & Cartigny, M.J.B. (2014) Supercritical and subcritical turbidity currents and their deposits—a synthesis. *Geology*, *42*, 987–990.

Prélat, A., Hodgson, D.M. & Flint, S.S. (2009) Evolution, architecture and hierarchy of distributary deep-water deposits: a high-resolution outcrop investigation from the Permian Karoo Basin, South Africa. *Sedimentology*, *56*, 2132–2154.

Pyles, D.R., Straub, K.M. & Stammer, J.G. (2013) Spatial variations in the composition of turbidites due to hydrodynamic fractionation. *Geophysical Research Letters*, *40*, 3919–3923.

Ragusa, J. & Kindler, P. (2018) Compositional variations in deep-sea gravity-flow deposits. A case study from the Voirons Flysch (Voirons-Wägital complex, Chablais Prealps, France). *Sedimentary Geology*, *377*, 111–130.

Rebesco, M., Hernández-Molina, F.J., Van Rooij, D. & Wåhlin, A. (2014) Contourites and associated sediments controlled by deep-water circulation processes: state-of-the-art and future considerations. *Marine Geology*, *352*, 111–154.

Romans, B.W., Castelltort, S., Covault, J.A., Fildani, A. & Walsh, J.P. (2016) Environmental signal propagation in sedimentary systems across timescales. *Earth-Science Reviews*, *153*, 7–29.

Ronda, A.C., Arias, A.H., Oliva, A.L. & Marcovecchio, J.E. (2019) Synthetic microfibers in marine sediments and surface seawater from the Argentinean continental shelf and a marine protected area. *Marine Pollution Bulletin*, *149*, 110618.

Rouse, H. (1937) Modern conceptions of the mechanics of fluid turbulence. *Transactions of the American Society of Civil Engineers*, *102*, 463–505.

Saller, A., Lin, R. & Dunham, J. (2006) Leaves in turbidite sands: the main source of oil and gas in the deep-water Kutei Basin, Indonesia. *American Association of Petroleum Geologists Bulletin*, *90*, 1585–1608.

Sanchez-Vidal, A., Thompson, R.C., Canals, M. & de Haan, W.P. (2018) The imprint of microfibres in southern European deep seas. *PLoS One*, *13*, e0207033.

Sarnthein, M. & Bartolini, C. (1973) Grain size studies on turbidite components from Tyrrhenian deep sea cores. *Sedimentology*, *20*, 425–436.

Schlining, K., von Thun, S., Kuhnz, L., Schlining, B., Lundsten, L., Jacobsen Stout, N., Chaney, L. & Connor, J. (2013) Debris in the deep: using a 22-year video annotation database to survey marine litter in Monterey Canyon, central California, USA. *Deep Sea Research Part I: Oceanographic Research Papers*, *79*, 96–105.

Shanmugam, G., Spalding, T.D. & Rofheart, D.H. (1993) Process sedimentology and reservoir quality of deep-marine bottom-current reworked sands (sandy contourites): an example from the Gulf of Mexico. *American Association of Petroleum Geologists Bulletin*, *77*, 1241–1259.

Shields, A. (1936) Anwendung der Aehnlichkeitsmechanig und der Turbulenzforschung auf die Geschiebebewegung. Technische Hochschule Berlin, 25 pp.

Sickmann, Z.T., Chheda, T.D., Capaldi, T.N., Thomson, K.D., Paull, C.K. & Graham, S.A. (2019) Using provenance analysis in an Anthropocene natural laboratory. *Quaternary Science Reviews*, *221*, 105890.

Sickmann, Z.T., Paull, C.K. & Graham, S.A. (2016) Detrital-zircon mixing and partitioning in fluvial to deep marine systems, Central California, U.S.A. *Journal of Sedimentary Research*, *86*, 1298–1307.

Sohn, Y.K. (1997) On traction-carpet sedimentation. *Journal of Sedimentary Research*, *67*, 502–509.

Soutter, E.L., Bell, D., Cumberpatch, Z.A., Ferguson, R.A., Spychala, Y.T., Kane, I.A. & Eggenhuisen, J.T. (2021) The influence of confining topography orientation on experimental turbidity currents and geological implications. *Frontiers in Earth Science*, *8*, 620.

Spychala, Y.T., Eggenhuisen, J.T., Tilston, M. & Pohl, F. (2020) The influence of basin setting and turbidity current properties on the dimensions of submarine lobe elements. *Sedimentology*, *67*, 3471–3491.

Spychala, Y.T., Hodgson, D.M., Prélat, A., Kane, I.A., Flint, S.S. & Mountney, N.P. (2017) Frontal and lateral submarine lobe fringes: comparing facies, architecture and flow processes. *Journal of Sedimentary Research*, *87*, 1–21.

Spychala, Y.T., Ramaaker, T.A.B., Eggenhuisen, J.T., Grundvåg, S.A., Pohl, F. & Wroblewska, S. (2021) Proximal to distal grain-size distribution of basin-floor lobes: a study from the Battfjellet Formation, Central Tertiary Basin, Svalbard. *Sedimentology*, *67*, 3471–3491.

Steel, E., Buttles, J., Simms, A.R., Mohrig, D. & Meiburg, E. (2017) The role of buoyancy reversal in turbidite deposition and submarine fan geometry. *Geology*, *45*, 35–38.

Stevenson, C.J., Feldens, P., Georgiopoulou, A., Schönke, M., Krastel, S., Piper, D.J.W., Lindhorst, K. & Mosher, D. (2018) Reconstructing the sediment concentration of a giant submarine gravity flow. *Nature Communications*, *9*, 2616.

Stevenson, C.J., Talling, P.J., Sumner, E.J., Masson, D.G., Frenz, M. & Wynn, R. (2014) On how thin submarine flows transported large volumes of sand for hundreds of kilometres across a flat basin plain without eroding the sea floor. *Sedimentology*, *61*, 1982–2019.

Stow, D.A.V., Amano, K., Balson, P.S., Brass, G.W., Corrigan, J., Raman, C.V., Tiercelin, J., Townsend, M. & Wijayananda, N.P. (1990) Sediment facies and processes on the distal Bengal Fan, Leg 116. In: Cochran, J.R. & Stow, D.A.V. (Eds.) *Proceedings of the ocean drilling project, Leg 116: Ocean drilling program scientific results 116*. College Station, TX: Ocean Drilling Program, pp. 377–396.

Stow, D.A.V. & Lovell, J.P.B. (1979) Contourites: their recognition in modern and ancient sediments. *Earth-Science Reviews*, *14*, 251–291.

Straub, K.M., Mohrig, D., McElroy, B., Buttles, J. & Pirmez, C. (2008) Interactions between turbidity currents and topography in aggrading sinuous submarine channels: a laboratory study. *Geological Society of America Bulletin*, *120*, 368–385.

Sumner, E.J., Amy, L.A. & Talling, P.J. (2008) Deposit structure and processes of sand deposition from decelerating sediment suspensions. *Journal of Sedimentary Research*, *78*, 529–547.

Sylvester, Z. & Lowe, D.R. (2004) Textural trends in turbidites and slurry beds from the Oligocene flysch of the East Carpathians, Romania. *Sedimentology*, *51*, 945–972.

Talling, P.J., Malgesini, G. & Felletti, F. (2013) Can liquefied debris flows deposit clean sand over large areas of sea floor? Field evidence from the Marnoso-arenacea Formation, Italian Apennines. *Sedimentology*, *60*, 720–762.

Talling, P.J., Masson, D.G., Sumner, E.J. & Malgesini, G. (2012) Subaqueous sediment density flows: depositional processes and deposit types. *Sedimentology*, *59*, 1937–2003.

Thompson, R.C., Olsen, Y., Mitchell, R.P., Davis, A., Rowland, S.J., John, A.W.G., McGonigle, D. & Russell, A.E. (2004) Lost at sea: where is all the plastic? *Science*, *304*, 838.

Tunis, G. & Uchman, A. (1996) Ichnology of eocene flysch deposits of the Istria peninsula, croatia and slovenia. *Ichnos*, *5*, 1–22.

Twichell, D.C., Schwab, W.C., Nelson, C.H., Kenyon, N.H. & Lee, H.J. (1992) Characteristics of a sandy depositional lobe on the outer Mississippi fan from SeaMARC IA sidescan sonar images. *Geology*, *20*, 689–692.

Uchman, A., Janbu, N.E. & Nemec, W. (2004) Trace fossils in the Cretaceous-Eocene flysch of the Sinop-Boyabat Basin, Central Pontides, Turkey. *Annales Societatis Geologorum Poloniae*, *74*, 197–235.

Udden, J.A. (1914) Mechanical composition of clastic sediments. *Geological Society of America Bulletin*, *25*, 655–744.

van Rijn, L.C. (1984) Sediment transport, part I: bed load transport. *Journal of hydraulic engineering*, *110*, 1431–1456.

van Rijn, L.C. (1993) *Principles of sediment transport in rivers, estuaries and coastal seas*. Amsterdam: Aqua Publications, 1200 pp.

Vianello, A., Boldrin, A., Guerriero, P., Moschino, V., Rella, R., Sturaro, A. & Da Ros, L. (2013) Microplastic particles in sediments of Lagoon of Venice, Italy: first observations on occurrence, spatial patterns and identification. *Estuarine, Coastal and Shelf Science*, *130*, 54–61.

Vrolijk, P.J. & Southard, J.B. (1997) Experiments on rapid deposition of sand from high-velocity flows. *Geosciences Canada 24*:1

Walker, R.G. (1966) Shale Grit and Grindslow shales; transition from turbidite to shallow water sediments in the upper Carboniferous of northern England. *Journal of Sedimentary Research*, *36*, 90–114.

Webb, M., Gough, A., Vannucchi, P., Lünsdorf, N.K. & McNeil, J. (2021) Sedimentary provenance of the Plio-Pleistocene Nicobar Fan: complex sourcing revealed through Raman spectroscopy heavy mineral analysis. *Marine and Petroleum Geology*, *125*, 104874.

Wentworth, C.K. (1922) A scale of grade and class terms for clastic sediments. *The Journal of Geology*, *30*, 377–392.

Woodall, L.C., Sanchez-Vidal, A., Canals, M., Paterson, G.L.J., Coppock, R., Sleight, V., Calafat, A., Rogers, A.D., Narayanaswamy, B.E., & Thompson, R.C. (2014) The deep sea is a major sink for microplastic debris. *Royal Society of Open Sciences*, *1*, 140317.

Zhong, G. & Peng, X. (2021) Transport and accumulation of plastic litter in submarine canyons—the role of gravity flows. *Geology*, *49*, 581–586. https://doi.org/10.1130/G48536.1

Zuffa, G.G., Cibin, U. & Di Giulio, A. (1995) Arenite petrography in sequence stratigraphy. *The Journal of Geology*, *103*, 451–459.

SUPPORTING INFORMATION

Additional supporting information may be found online in the Supporting Information section.

How to cite this article: Bell D, Soutter EL, Cumberpatch ZA, et al. Flow-process controls on grain type distribution in an experimental turbidity current deposit: Implications for detrital signal preservation and microplastic distribution in submarine fans. *Depositional Rec*. 2021;7:392–415. https://doi.org/10.1002/dep2.153